Journal Pre-proof

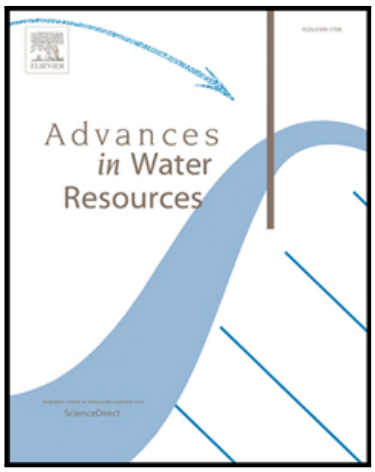

A new two-phase shallow water hydro-sediment-morphodynamic model based on the HLLC solver and the hybrid LTS/GMaTS approach

Peng Hu , Binghan Lyu , Ji Li , Mengzhe Sun , Wei Li , Zhixian Cao

PII: S0309-1708(22)00124-5
DOI: https://doi.org/10.1016/j.advwatres.2022.104254
Reference: ADWR 104254

To appear in: *Advances in Water Resources*

Received date: 5 December 2021
Revised date: 4 June 2022
Accepted date: 8 June 2022

Please cite this article as: Peng Hu , Binghan Lyu , Ji Li , Mengzhe Sun , Wei Li , Zhixian Cao , A new two-phase shallow water hydro-sediment-morphodynamic model based on the HLLC solver and the hybrid LTS/GMaTS approach, *Advances in Water Resources* (2022), doi: https://doi.org/10.1016/j.advwatres.2022.104254

Highlights

- A new two-phase model for sediment-laden flows is developed based on the HLLC solver and the LTS approach
- Application of the HLLC solver brings considerable improvement in numerical accuracy
- Implementation of the hybrid LTS/GMaTS leads to great reduction in the computational cost

A new two-phase shallow water hydro-sediment-morphodynamic model based on the HLLC solver and the hybrid LTS/GMaTS approach

Peng Hu[1,*] pengphu@zju.edu.cn, Binghan Lyu[2], Ji Li[3], Mengzhe Sun[4], Wei Li[5], Zhixian Cao[6]

[1]Ocean College, Zhejiang University, Zhoushan Campus, 316021, China

[2]Research Assistant, Ocean College, Zhejiang University, Zhoushan Campus, 316021, China

[3]Lecturer, Faculty of Science and Engineering, Swansea University, Swansea, SA1 8EN, UK

[4]Ocean College, Zhejiang University, Zhoushan Campus, 316021, China

[5]Ocean College, Zhejiang University, Zhoushan Campus, 316021, China

[6]State Key Laboratory of Water Resources and Hydropower Engineering Science, Wuhan University, Wuhan, 430000, China

[*]Corresponding author

Abstract

In this paper, we present a new computationally-efficient and high-resolution depth-averaged two-phase flow model for hydro-sediment-morphydynamic processes, featuring an advance over existing models in terms of accuracy and efficiency of numerical solution. Under the framework of finite volume method (FVM) on unstructured grids, the Harten-Lax-van Leer-Contact (HLLC) approximate Riemann solver is proposed to compute inter-cell fluxes by applying the classical upwind HLLC approach to the water-sediment mixture and the sediment phases separately, in contrast to previous two-phase flow models using centered

schemes. Moreover, to improve computational efficiency, the local-time-stepping (LTS) approach is implemented, the first attempt in the field of two-phase flow modelling. After a convergence rate study, the model is tested against a series of flow-sediment-bed evolutions induced by (1) two refilling processes of dredged trenches, (2) two instantaneous dam-break flooding flows, and (3) one levee breaching process by overtopping flows. It features encouraging performance when compared to a two-phase flow model based on a centered scheme and global time bound, characterized by more accurate results and much less computational cost. The present modelling framework shows promise in practical shallow water hydro-sediment-morphodynamic modelling applications.

Keywords

hydro-sediment-morphodynamic process; two-phase flow modeling; HLLC Riemann solver; Local-time-step; Globally maximum-time-step

1. Introduction

Refined and efficient modelling of shallow water hydro-sediment flows is important for not only river engineering practice, but also flood risk management. The last two decades have witnessed increasingly widespread applications of shallow water (depth-averaged) hydro-sediment-morphodynamic (SHSM) models and their variants (Cao et al. 2017). However, existing SHSM models are mostly based on the single-phase premise (Hoey and Ferguson, 1994; Armanini and DiSilvio, 1998; Cao et al. 2011, 2017; Guy and Castelltort, 2006; Wu and Wang, 2008; Canestrelli and Toro, 2012; Hu et al. 2012, 2014, 2018, 2019; Juez et al. 2014; Zhao et al. 2019; Meurice and Soares-Frazão, 2020). In these models, the velocities of

the sediment phases are assumed equal to the mixture velocity or are empirically determined by the mixture velocity along with a modification coefficient less than unity. Consequently, the relative motions and interactions between water and sediment phases are not incorporated. In fact, not only is the advection velocity of bedload appreciably lower than the flow (Greimann et al. 2008), but also a velocity lag between the flow and the suspended sediments has been observed (Muste et al. 2005). In this regard, a two-phase model is certainly warranted.

There have been different types of two-phase models for shallow water hydro-sediment flows. For example, vertical 2D two-phase models were used to investigate the vertical sediment concentration distributions (Bakhtyar et al. 2009; Chen et al. 2011); meshfree SPH two-phase models were used to tackle problems with strong free surface variations (Shi et al. 2017, 2019); the two-phase SHSM models, which are the present topic, have been developed for not only fluvial processes (Greco et al. 2012; Di Crisco et al. 2016; Li et al. 2018, 2019, 2020), but also earth surface flows such as debris flows and granular flows (e.g., Pitman and Le, 2005; Pudasaini, 2012). It is appreciated that bedload occurs mainly in a thin layer on the top of the erodible bed surface, where the sediment concentration is much higher than the depth-averaged value. In this regard, a two-layer two-phase model may also be appealing (Zech et al. 2008; Martínez-Aranda et al. 2019), which is reserved for future study. Unless otherwise stated, the present two-phase SHSM models are all depth-averaged versions. In the last decades, the shock-capturing finite volume method has been widely used to deal with shallow water modeling challenges such as wet/dry treatments, capturing shock/contact

discontinuities (Greco et al. 2012; Di Crisco et al. 2016; Li et al. 2018, 2019, 2020). However, existing two-phase SHSM models have still suffered from two major shortcomings. First, existing two-phase SHSM models exclusively employ the centered schemes or more simplified method to estimate the inter-cell numerical flux (Greco et al. 2012; Di Crisco et al. 2016; Li et al. 2018, 2019, 2020). While using a centered scheme avoids the difficulty of managing complex wave structures by minimizing the use of eigenvalues, they tend to spread the solution more than upwind schemes (e.g., the HLLC Riemann solver and the Roe Riemann solver). In particular, when multi-dimensional problems are studied, vortices are excessively dissipated by numerical diffusion, as well as any shear flow (Canestrelli and Toro 2012). Moreover, when passive scalars are conveyed, centered schemes may also spread the solution. The HLLC Riemann solver, which represents a classical upwind scheme by making full use of the eigen-structures, will be adopted for the present two-phase SHSM model. A major challenge for applying the HLLC solver in two-phase SHSM models is their complex eigen-structures arising from the additional momentum equations of the sediment phases. Briefly, the HLLC Riemann solver was developed for 3-wave Riemann structures (Toro, 2001, 2019), whereas the two-phase flow model, even if a single-sized sediment transport is assumed, would produce 6 wave speeds and 7 Riemann fields. Moreover, if the momentum source terms are included into the Riemann structures, an additional stationary wave may appear (Murillo and García-Navarro, 2012). Furfaro and Saurel (2015) also appreciated the difficulty for applying the HLLC solver to the compressible fluid-fluid two phase flows that have seven wave speeds. Furfaro and Saurel (2015) proposed to use the HLLC solver

separately for different phases because each fluid phase has its own set of mass, momentum and energy balancing equations. This strategy is extended to present two-phase SHSM model. Specifically, the entire system is split into a mixture part and several parts of different sediment sizes, facilitating usage of the HLLC solver.

Second, the attractiveness of existing two-phase SHSM models is limited by its relatively high computational cost. Specifically, existing two-phase SHSM models have employed the globally minimum time step (GMiTS) for variable updating. That is, the globally minimum value of all locally allowable maximum time steps, which are computed by the Courant–Friedrichs–Lewy (CFL) stability condition, is used. For most cells, however, the GMiTS is much smaller than the locally allowable maximum time steps. In contrast to the GMiTS, an alternative appealing method is the hybrid local-time-step (LTS)/globally maximum time step (GMaTS). By this hybrid approach, updating of the hydro-sediment module is completed by using local time steps close to the locally maximum time steps as much as possible (Sanders, 2008), whereas updating of the morphodynamic model is completed by using the GMaTS. It has been demonstrated that this hybrid approach can bring significant reduction in the computational cost of quasi-single phase SHSM models (Hu et al. 2019). However, it has been rarely reported for two-phase SHSM models. Furthermore, GPU-acceleration is also an important option for improving the computational efficiency (Ingelsten et al. 2020; Conde et al. 2020; Martínez-Aranda et al. 2022; Sweet et al. 2018), which is reserved for future study.

This paper presents a new computationally-efficient and high-resolution depth-averaged two-phase model for hydro-sediment-morphodynamic processes. Mathematical formulations are

presented in Section 2. Specifically, the governing equations are solved by the finite volume method on unstructured triangular cells. The inter-cell numerical flux is estimated by the HLLC solver, which is novel as compared to previous two-phase SHSM models that are mostly based on centered schemes. For variable updating, the hybrid LTS/GMaTS approach is implemented, which, to the authors' best knowledge, has rarely been reported for two-phase SHSM modelling. Moreover, the model is parallelized by using the OPEN MP technique. In Section 3, the convergence rate studies are firstly conducted; afterwards, the new two-phase SHSM model is tested against a series of flow-sediment-bed evolutions due to (1) two refilling processes of dredged trenches, (2) two instantaneous dam-break flooding flows, and (3) one levee breaching process by overtopping flows. Particular attention is given to its improved quantitative accuracy and enhanced computational efficiency, as compared to previous two-phase SHSM models (Greco et al. 2012; Di Cristo et al. 2016). The paper is concluded in Section 4.

2. Mathematical formulations

2.1 Governing equations and empirical closures

Consider shallow water-sediment flows over an erodible bed composed of non-cohesive sediment with $NSPS$ size classes. Let d_k denote the diameter of the k-th sediment size, where subscript $k=1,2,.....,NSPS$. The proposed model is a two-dimensional extension of the one-dimensional depth-averaged two-phase flow model (Li et al. 2019). The governing equations comprise mass and momentum conservation equations for the water-sediment mixture, the sediment phases, and the mass conservation equations for the bed material. The

resulting system of equations can be expressed in standard, well-structured conservation form as follows:

$$\frac{\partial \mathbf{U}}{\partial t}+\frac{\partial \mathbf{F}}{\partial x}+\frac{\partial \mathbf{G}}{\partial y}=\mathbf{S}_b+\mathbf{S}_\tau+\mathbf{S}_f+\mathbf{S}_m+\mathbf{S}_s \quad (1)$$

$$\mathbf{U}=\begin{bmatrix} h \\ hu \\ hv \\ hc_k \\ hc_k u_{sk} \\ hc_k v_{sk} \end{bmatrix}, \mathbf{F}=\begin{bmatrix} hu \\ hu^2+gh^2/2 \\ huv \\ hu_{sk}c_k \\ hc_k {u_{sk}}^2+\dfrac{\rho c_k g h^2}{2\rho_s} \\ hc_k u_{sk} v_{sk} \end{bmatrix}, \mathbf{G}=\begin{bmatrix} hv \\ huv \\ hv^2+gh^2/2 \\ hv_{sk}c_k \\ hc_k u_{sk} v_{sk} \\ hc_k {v_{sk}}^2+\dfrac{\rho c_k g h^2}{2\rho_s} \end{bmatrix},$$

$$\mathbf{S}_b=\begin{bmatrix} 0 \\ ghS_{bx} \\ ghS_{by} \\ 0 \\ \dfrac{\rho g h c_k S_{bx}}{\rho_s} \\ \dfrac{\rho g h c_k S_{by}}{\rho_s} \end{bmatrix}, \mathbf{S}_\tau=\begin{bmatrix} 0 \\ \dfrac{-\tau_{bx}}{\rho} \\ \dfrac{-\tau_{by}}{\rho} \\ 0 \\ \dfrac{-\tau_{skbx}}{\rho_s} \\ \dfrac{-\tau_{skby}}{\rho_s} \end{bmatrix}, \mathbf{S}_f=\begin{bmatrix} N_m \\ N_{mx} \\ N_{my} \\ 0 \\ N_{skx} \\ N_{sky} \end{bmatrix}, \mathbf{S}_m=\begin{bmatrix} F \\ -\dfrac{(\rho_0-\rho)uF}{\rho} \\ -\dfrac{(\rho_0-\rho)vF}{\rho} \\ E_k-D_k \\ 0 \\ 0 \end{bmatrix}, \mathbf{S}_s=\begin{bmatrix} 0 \\ -\dfrac{Rgh^2}{2}\dfrac{\partial C}{\partial x} \\ -\dfrac{Rgh^2}{2}\dfrac{\partial C}{\partial y} \\ 0 \\ \dfrac{1}{2}gh^2\dfrac{\partial c_k}{\partial x} \\ \dfrac{1}{2}gh^2\dfrac{\partial c_k}{\partial y} \end{bmatrix} \quad (2)$$

and bed deformation equation:

$$\frac{\partial z_b}{\partial t}=\frac{D_T-E_T}{1-p_0} \quad (3)$$

as well as the active layer equation:

$$\frac{\partial(\delta f_{ak})}{\partial t}=\frac{D_k-E_k}{1-p_0}-f_{sk}\frac{\partial \eta}{\partial t} \quad (4)$$

where $\mathbf{U}$ represents the vector of the conserved variables; $\mathbf{F},\mathbf{G}$ are the vectors of the flux variables; $\mathbf{S}_b$ denotes the vector of the bed slope; $\mathbf{S}_\tau$ denotes the vector of the friction source terms; $\mathbf{S}_f$ is the vector containing physically-based contributions from the interactions between the water and sediment phases and sediment-sediment phases; $\mathbf{S}_m$ is the vector of the source terms representing mass and momentum contributions from bed exchange; and $\mathbf{S}_s$

is the vector of the source terms representing momentum contributions derived of decoupling the flow density from the mass and momentum conservative variables; t is the time; x, y are the spatial horizontal coordinates in the Cartesian coordinate system; h is the depth of the water-sediment mixture; z_b is the bed elevation; g = 9.8 m^2/s is the gravitational acceleration; u, v are the depth-averaged velocities of the water-sediment mixture in the $x-$ and $y-$directions respectively; u_{sk}, v_{sk} are the depth-averaged size-specific velocities of the sediment phase in the $x-$ and $y-$ directions ; c_k is the depth-averaged size-specific volumetric sediment concentration; $R = (\rho_s - \rho_f)/\rho$; $\rho = \rho_f(1-C) + \rho_s C$ is the density of the water-sediment mixture; ρ_f = 1000 kg/m^3 and ρ_s are the densities of water and sediment respectively; $C = \sum c_k$ is the depth-averaged total sediment concentration; $S_{bx} = -\partial z_b / \partial x$, $S_{by} = -\partial z_b / \partial y$ are the bed slopes in the $x-$ and $y-$ directions; $\tau_{bx} = \tau_{fbx} + \sum \tau_{skbx}$ and $\tau_{by} = \tau_{fby} + \sum \tau_{skby}$ are the total bed shear stresses for the hydro-sediment mixture, by which the total bed shear stresses for the water-sediment mixture are divided into the bed shear stress components exerted respectively on the water and sediment phases; τ_{fbx} and τ_{fby} are the bed resistance stresses for the water phase in the $x-$ and $y-$directions; τ_{skbx}, τ_{skby} are the bed shear stresses for sediment phases in the $x-$ and $y-$directions; $F = (E_T - D_T)/(1-p_0)$; $E_T = \sum E_k$ and $D_T = \sum D_k$ are the total sediment entrainment and deposition fluxes; E_k and D_k are the size-specific sediment entrainment and deposition fluxes; p_0 is the bed sediment porosity; $\eta = z_b - \delta$ is the bottom elevation of the active layer, $\delta = a_h d_{84}$ is the thickness of the active layer, a_h is an empirical coefficient ranging from 1 to 4, d_{84} is a characteristic sediment size, the subscript 84 means that 84% sediments are finer than d_{84}; f_{ak} is the sediment fractions within the bed active layer; f_{sk} is the sediment fractions at the interface

between the active layer and those below the active layer. $N_m, N_{mx}, N_{my}, N_{skx}, N_{sky}$ are components of the vector $\mathbf{S}_f$, which are expressed as follows:

$$N_m = \frac{\rho_s - \rho_f}{\rho_f} \sum \left(\left[\frac{\partial h c_k (u - u_{sk})}{\partial x} \right] + \left[\frac{\partial h c_k (v - v_{sk})}{\partial y} \right] \right) \tag{5a}$$

$$N_{mx} = -\frac{1}{\rho} \frac{\partial}{\partial x} h \sum [\rho_s c_k i_{s_k x} (i_{s_k x} - i_{fx})] - \frac{1}{\rho} \frac{\partial}{\partial y} h \sum [\rho_s c_k i_{s_k x} (i_{s_k y} - i_{fy})] \tag{5b}$$

$$N_{my} = -\frac{1}{\rho} \frac{\partial}{\partial y} h \sum [\rho_s c_k i_{s_k y} (i_{s_k y} - i_{fy})] - \frac{1}{\rho} \frac{\partial}{\partial x} h \sum [\rho_s c_k i_{s_k y} (i_{s_k x} - i_{fx})] \tag{5c}$$

$$N_{skx} = \frac{1}{\rho_s} (F_{skfx} + F_{s-skx}) \tag{5d}$$

$$N_{sky} = \frac{1}{\rho_s} (F_{skfy} + F_{s-sky}) \tag{5e}$$

where $\rho_0 = \rho_f p_0 + \rho_s (1 - p_0)$ is the density of bed materials; $i_{s_k x} = u_{sk} - u$, $i_{s_k y} = v_{sk} - v$ are inter-phase velocity discrepancy between the size-specific sediment phase and the water-sediment mixture; $i_{fx} = u_f - u$, $i_{fy} = v_f - v$ denote velocity discrepancy between the water phase and the water-sediment mixture; u_f and v_f are the depth-averaged velocity of the water phase (Eq. 6); $F_{skfx} = \rho_f D_{rk} h (u_f - u_{sk})$, $F_{skfy} = \rho_f D_{rk} h (v_f - v_{sk})$ are the size-specific depth-averaged interphase interaction forces; D_{rk} is a function related to the drag coefficient (see Eq. 7); F_{s-skx} and F_{s-sky} are the size-specific depth-averaged particle-particle interactive drag forces (Eq. 8):

$$u_f = (\rho u - \sum \rho_s u_{sk} c_k) / (\rho_f (1 - C)) \tag{6a}$$

$$v_f = (\rho v - \sum \rho_s v_{sk} c_k) / (\rho_f (1 - C)) \tag{6b}$$

$$D_{rk}=\begin{cases}\dfrac{150c_k^2\nu_{\mu f}}{\left(1-\sum c_k\right)d_k^2}+\dfrac{7c_k}{4d_k}\sqrt{(u_f-u_{sk})^2+(v_f-v_{sk})^2} & if\ (c_k\geq 0.2)\\ \dfrac{3C_d\left(1-\sum c_k\right)c_k}{4d_k}\left(1-\sum c_k\right)^{-2.65}\sqrt{(u_f-u_{sk})^2+(v_f-v_{sk})^2} & if\ (c_k<0.2)\end{cases} \tag{7a}$$

$$C_d=\begin{cases}\dfrac{24\ (1+0.15\mathrm{R}_{ek}^{\ 0.687})}{\mathrm{R}_{ek}} & if\ (\mathrm{R}_{ek}<1000)\\ 0.44 & if\ (\mathrm{R}_{ek}\geq 1000)\end{cases} \tag{7b}$$

$$F_{s-skx}=\frac{1}{2}C\rho gh^2c_k\frac{\partial}{\partial x}(\frac{c_k}{C})-\rho_s\frac{c_k}{C}c_{sd}(u_{sk}-\bar{u}_s)hc_k-\rho_s\nu_d hc_k\frac{\partial}{\partial x}(\frac{c_k}{C}) \tag{8a}$$

$$F_{s-sky}=\frac{1}{2}C\rho gh^2c_k\frac{\partial}{\partial y}(\frac{c_k}{C})-\rho_s\frac{c_k}{C}c_{sd}(v_{sk}-\bar{v}_s)hc_k-\rho_s\nu_d hc_k\frac{\partial}{\partial y}(\frac{c_k}{C}) \tag{8b}$$

where $\mathrm{R}_{ek}=(1-C)\sqrt{(u_f-u_{sk})^2+(v_f-v_{sk})^2}d_k/\nu_{\mu f}$; $\nu_{\mu f}=10^{-6}\ m^2/s$ is the kinematic viscosity of fluid phase; $c_{sd}=6.3\ \mathrm{s}^{-1}$ is the liner drag coefficient; $\nu_d=1.26\times10^{-5}\ \mathrm{m}^2/\mathrm{s}^2$ is the linear diffusive coefficient (Hill and Tan, 2014); $\bar{u}_s=\sum c_k u_{sk}/C$, $\bar{v}_s=\sum c_k v_{sk}/C$ are mean sediment velocity. By Eq. (7), the interphase drag force is determined by combining the Ergun equation for dense water-sediment mixtures and the power law for dilute suspensions (Gidaspow, 1994); By Eq. (8), the inter-grain size interaction force includes a linear velocity-dependent drag force, an inter-grain size surface interaction force and a remixing force (Gray and Chugunov, 2006; Hill and Tan, 2014). Eqs. (9, 10) present empirical relations for bed resistance from the water phase (using the Manning roughness) and for the sediment phase (using the Coulomb friction law, Savage and Hutter, 1989), respectively:

$$\tau_{fbx}=\rho_f g\frac{n^2u_f\sqrt{u_f^{\ 2}+v_f^{\ 2}}}{h_f^{\ 1/3}},\tau_{fby}=\rho_f g\frac{n^2v_f\sqrt{u_f^{\ 2}+v_f^{\ 2}}}{h_f^{\ 1/3}} \tag{9}$$

$$\tau_{skbx}=(\rho_s-\rho_f)ghc_k\tan\phi_{bed}\frac{u_{sk}}{\sqrt{u_{sk}^2+v_{sk}^2}},\tau_{skby}=(\rho_s-\rho_f)ghc_k\tan\phi_{bed}\frac{v_{sk}}{\sqrt{u_{sk}^2+v_{sk}^2}} \tag{10}$$

where n is the Manning roughness; $h_f=h(1-C)$ is the depth of the water phase; the parameter $\tan\phi_{bed}$ expresses the collinearity of shear stress and normal stress; ϕ_{bed} is s the friction angle of the sheared granular material. While it has been demonstrated that the dynamic pore-fluid pressure, i.e. the excess of pressure within the liquid phase respect to the

hydrostatic value, is important for very dense-packed water-solid flows (McArdell et al. 2007, Iverson et al. 2010) such as debris flows (Hungr and Mcdougall, 2009; George and Iverson, 2014), the present study used the Coulomb-relation (Savage and Hutter, 1989) for the sediment resistance, which expresses the collinearity of shear stress and normal stress through a friction coefficient. This relation implicitly indicates that the pressure within the liquid phase at the bed surface is hydrostatic, which is reasonable because in the present cases, all sediment volume concentrations are below 0.1. Sediment exchange with the bed is estimated by Eqs. (11)

$$D_k = \alpha_k c_k \omega_k, E_k = \alpha_k c_{ek} \omega_k, \tag{11}$$

where ω_k is the settling velocity for sediment of diameter d_k, which is calculated using the Zhang (1961) formulation; c_{ek} is the size specific depth-averaged sediment transport capacity, of which the estimation will be introduced in the specific case study; and the parameter α_k represents the difference between the near-bed concentration and the depth-averaged concentration is estimated with an upper limit $\alpha_k \le h/\omega_k \Delta t$ derived by Hu et al. (2014). Eq. (12) presents empirical relation for the fraction f_{sk} at the lower boundary of the active layer (Hoey and Ferguson, 1994)

$$f_{sk} = \begin{cases} f_{sk}^0 & \partial\eta/\partial t < 0 \\ f_{ak} & \partial\eta/\partial t > 0 \end{cases} \tag{12}$$

where f_{sk}^0 is the sediment fraction of the k-th size sediment in the substrate layer.

2.2 Time step estimations

Fig. 1 shows sketches of internal triangular cells: a triangular cell has three nodes, three faces, and three neighboring cells (Fig. 1a) and a face has two nodes and is shared by two neighboring cells (Fig. 1b). The total number of cells is N_c and the total number of faces is N_f; In Fig. 1a, R_{ij} is the distance from cell-i center to its j-th face, where the i indicates

the sequence of the cells and j indicates the j-th face of the cell i with $j=1,2,3$; A_i is the area of the cell-i; ΔL_{ij} is the length of the j-th face of the cell-i; $\mathbf{n}_{ij}=(n_x,n_y)_{ij}$ represents the normal outward direction of the j-th face of the cell-i. Physical conserved variables shown in Fig.1 will be introduced when they appear in the mathematical formulations below.

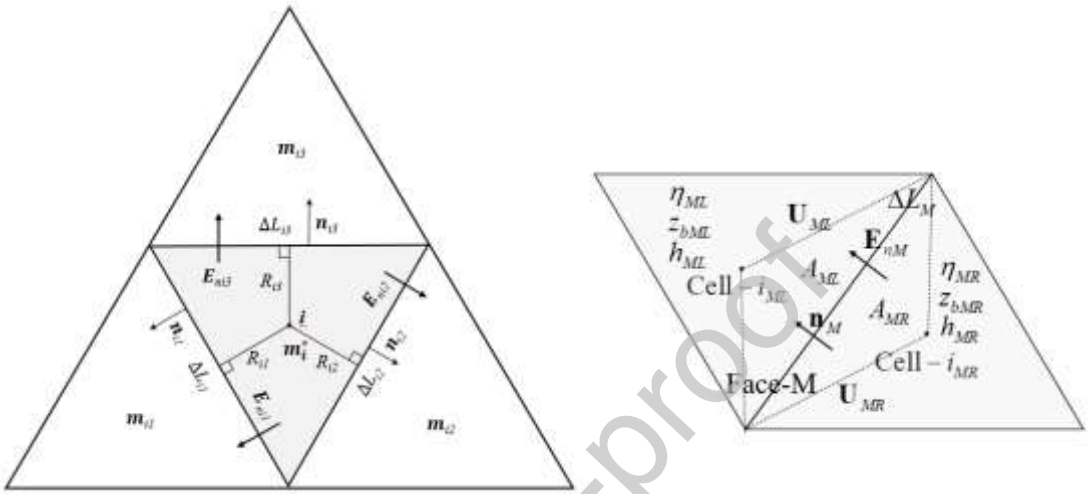

Figure 1. Sketches of the unstructured triangular meshes: (a) a cell surrounded by three cells and (b) a face shared by two neighboring cells

The locally allowable maximum time step Δt_{ami} (where the subscript 'am' indicates allowable maximum) is firstly estimated as follows:

$$\Delta t_{\mathrm{ami}}=Cr\min_{\substack{j=1,2,3\\k=1,\ldots,NSPS}}\left(\frac{R_{ij}}{\sqrt{u_{ij}^2+v_{ij}^2}+\sqrt{gh_i}},\frac{R_{ij}}{\sqrt{u_{skij}^2+v_{skij}^2}+\sqrt{0.5\rho_i gh_i/\rho_s}}\right),\quad i=1,2,3,\sim,N_c \tag{13}$$

where Cr is the Courant number, which is set as 0.9 in this paper; and h_i,ρ_i are the depth and the density for the hydro-sediment mixture at cell-i. $u_{ij},v_{ij},u_{skij},v_{skij}$ are velocities of the j-th face of the cell-i. Traditional models always use the globally minimum time step Δt_{Gmi} to update the physical variables and here we use the approach of the local graded time step presented by Hu et al. (2019). The potential graded LTS level for every cell is computed as:

$$m_i = \min\left(\text{int}(\frac{\log(\Delta t_{ami} / \Delta t_{Gmi})}{\log(2)}), m_{user} \right), \quad i = 1, 2, 3, \sim, N_c \tag{14a}$$

$$\Delta t_{Gmi} = \min_{i=1, N_c}(\Delta t_{ami}) \tag{14b}$$

where m_{user} is a user-defined upper limit value. Setting $m_{user} = 0$ means the graded levels of all cells are zero, which will make the model equivalent to the GMiTS model. The model further modifies the LTS level of neighboring cells that are characterized by abrupt flow regime changes (i.e. the wet/dry front and the static/dynamic front of both sediment and water). Specifically, LTS level of such neighboring cells are set to a locally minimum value. The actual grade level m_{fM} for face-M is computed as follows

$$m_{fM} = \min(m_{ML}, m_{MR}), \quad M = 1, 2, 3, \sim, N_f \tag{15}$$

where m_{ML}, m_{MR} represent the potential graded levels of two neighboring cells of face-M (see Fig. 1b). The potential graded time step level of each cell is finally computed in the following

$$m_i^* = \min(m_i, m_{i1}, m_{i2}, m_{i3}), i = 1, 2, 3, \sim, N_c \tag{16}$$

where m_{i1}, m_{i2}, m_{i3} represents the potential graded level of the three neighboring cells of cell-i. Afterwards, the graded local-time-step is computed as:

$$\Delta t_{L-i} = 2^{m_i^*} \Delta t_{Gmi}, i = 1, 2, 3, \sim, N_c \tag{17}$$

Finally the GMaTS can be computed as:

$$\Delta T = \max(\Delta t_{L-i}), i = 1, 2, 3, \sim, N_c \tag{18}$$

2.3 Finite volume discretization

As shown in Eqs. (19-21), the hybrid LTS/GMaTS approach is used for variable updating. Specifically, the hydro-sediment part is updated by the LTS and the morphodynamic part are updated by GMaTS (see Fig. 2 for a summary):

$$\mathbf{U}_i^{**} = \mathbf{U}_i^{*} - \frac{\Delta t_{L-i}}{A_i}\sum_{j=1}^{3}\mathbf{E}_{nij}^{*}\Delta L_{ij} + \Delta t_{L-i}(\bar{\mathbf{S}}_{bi} + \mathbf{S}_{\tau i}^{*} + \mathbf{S}_{fi}^{*} + \mathbf{S}_{mi}^{*} + \mathbf{S}_{si}^{*}) \tag{19}$$

$$(z_b)_i^{t_0+\Delta T} = (z_b)_i^{t_0} + \sum_{S_c=1}^{N_p}\frac{\Delta t_{L-i}[(D_T)_i^{Sc} - (E_T)_i^{Sc}]}{1-p_o} \tag{20}$$

$$(\delta f_{ak})_i^{t_0+\Delta T} = (\delta f_{ak})_i^{t_0} + \sum_{S_c=1}^{N_p}\frac{\Delta t_{L-i}[(D_k)_i^{Sc} - (E_k)_i^{Sc}]}{1-p_o} - f_{sk,i}\sum_{S_c=1}^{N_p}\frac{\Delta t_{L-i}[(D_T)_i^{Sc} - (E_T)_i^{Sc}]}{1-p_o} \tag{21}$$

where $\mathbf{E}_{nij}^{*} = \left(\mathbf{F}n_x + \mathbf{G}n_y\right)_{ij}$ is the numerical flux crossing the j-th face of the cell-i, which is estimated by approximate Riemann solvers (see Section 2.4); the superscripts '*' and '**' represents two consecutive sub-time levels (the temporal interval is Δt_{L-i}) between t_0 and $t_0 + \Delta T$. The temporal interval between the two synchronized time levels t_0 and $t_0 + \Delta T$ is termed a full cycle; $N_p = \Delta T / \Delta t_{Gmi}$ is the maximum number of sub-cycles in the full cycle; and the symbol S_c is used to indicate the sequence of sub-cycles with $S_c = 1, 2, \sim, N_p$. Within a full cycle, the hydro-sediment-morphodynamic system will be updated from one synchronized time level to the next. To complete such update, the morphodynamic part at all cells is updated only once (Eqs. 20, 21), whereas the times that the hydro-sediment part has to be updated at a specific cell-i is equal to the ratio $\Delta T / \Delta t_{L-i}$ (Eq. 19). If $\Delta t_{L-i} = 2^{m_i^*}\Delta t_{\min}$, the times that the hydro-sediment part at cell-i is updated are $N_p / 2^{m_i^*}$, indicating that hydro-sediment part in cell-i will be updated every $2^{m_i^*}$ sub-cycles. In a specific sub-cycle S_c, the

implementation of the hydro-sediment part is activated if this inequality $m_i^* < l_s(S_c)$ is satisfied, where l_s is a function of the sequence S_c (see Hu et al. (2019) for the function), whereas estimation of numerical fluxes in a specific sub-cycle depends on whether $\mathrm{MOD}\left((S_c-1)/2^{m_{fM}}\right)=0$. If the hydro-sediment part is to be updated in the S_c sub-cycle, the source terms would also be estimated; otherwise the source terms in the S_c sub-cycle take zero-value. Specifically, the source terms for the bed slope $\overline{\mathbf{S}}_{bi}$ are evaluated using the slope flux method (Hou et al. 2013) with flow variables at the sub-cycle but bed elevations at the initial synchronized time level 't_0' as input. The vectors $\mathbf{S}_{si}^*$, $\mathbf{S}_{\tau i}^*$, $\mathbf{S}_{fi}^*$ and $\mathbf{S}_{mi}^*$ are evaluated explicitly using empirical relations with flow variables at the time level after updating $\overline{\mathbf{S}}_{bi}$ and $\mathbf{E}_{nij}^*$ as input. To overcome numerical instabilities arising from the relatively large spatial and time steps that lead to an issue of stiff source term, the following numerical treatments are proposed to attach the implementation of theoretically-derived lower and upper limits for the inter-phase interactive forces. For updating momentum equations of hydro-sediment mixture, modified source term $\mathbf{S}_{xi}^{mixture*}=\mathbf{S}_{\tau i}^*(2)+\mathbf{S}_{si}^*(2)+\mathbf{S}_{fi}^*(2)$ and $\mathbf{S}_{yi}^{mixture*}=\mathbf{S}_{\tau i}^*(3)+\mathbf{S}_{si}^*(3)+\mathbf{S}_{fi}^*(3)$ in the x, y direction can be defined as:

$$\mathbf{S}_{xi}^{mixture*}=\begin{cases}\max[\mathbf{S}_{xi}^{mixture*},-h_i^*u_i^*/\Delta t_{L-i}] & u_i\geq 0\\ \min[\mathbf{S}_{xi}^{mixture*},-h_i^*u_i^*/\Delta t_{L-i}] & u_i<0\end{cases} \tag{22a}$$

$$\mathbf{S}_{yi}^{mixture*}=\begin{cases}\max[\mathbf{S}_{yi}^{mixture*},-h_i^*v_i^*/\Delta t_i] & v_i^*\geq 0\\ \min[\mathbf{S}_{yi}^{mixture*},-h_i^*v_i^*/\Delta t_i] & v_i^*<0\end{cases} \tag{22b}$$

For updating momentum equations of sediment phase with the size d_k, modified source term can be defined as:

$$\mathbf{S}_{xi}^{sed*}(k)=\begin{cases}\max[\mathbf{S}_{xi}^{sed*}(k),-(hc_k u_{sk})_i^*/\Delta t_{L-i}] & u_{ski}^*\geq 0\\ \min[\mathbf{S}_{xi}^{sed*}(k),-(hc_k u_{sk})_i^*/\Delta t_{L-i}] & u_{ski}^*<0\\ \min[\mathbf{S}_{xi}^{sed*}(k),((hc_k u_f)_i^{**}-(hc_k u_{sk})_i^*)/\Delta t_{L-i}] & u_{ski}^*\geq 0\\ \max[\mathbf{S}_{xi}^{sed*}(k),((hc_k u_f)_i^{**}-(hc_k u_{sk})_i^*)/\Delta t_{L-i}] & u_{ski}^*<0\end{cases}. \tag{23a}$$

$$\mathbf{S}_{yi}^{sed*}(k)=\begin{cases}\max[\mathbf{S}_{yi}^{sed*}(k),-(hc_k v_{sk})_i^*/\Delta t_{L-i}] & v_{ski}^*\geq 0\\ \min[\mathbf{S}_{yi}^{sed*}(k),-(hc_k v_{sk})_i^*/\Delta t_{L-i}] & v_{ski}^*<0\\ \min[\mathbf{S}_{yi}^{sed*}(k),((hc_k v_f)_i^{**}-(hc_k v_{sk})_i^*)/\Delta t_{L-i}] & v_{ski}^*\geq 0\\ \max[\mathbf{S}_{yi}^{sed*}(k),((hc_k v_f)_i^{**}-(hc_k v_{sk})_i^*)/\Delta t_{L-i}] & v_{ski}^*<0\end{cases} \tag{23b}$$

For the subcritical inflowing boundary face, the unit discharge and unit-width sediment transport rate (or the sediment concentration) must be given. The tangential velocity to the face is set to zero. The water depth and the normal flow velocities are estimated by the method of characteristics. For supercritical outlet boundary face and a wall boundary face, all physical variables at the face are set equal to the values at the neighboring cell.

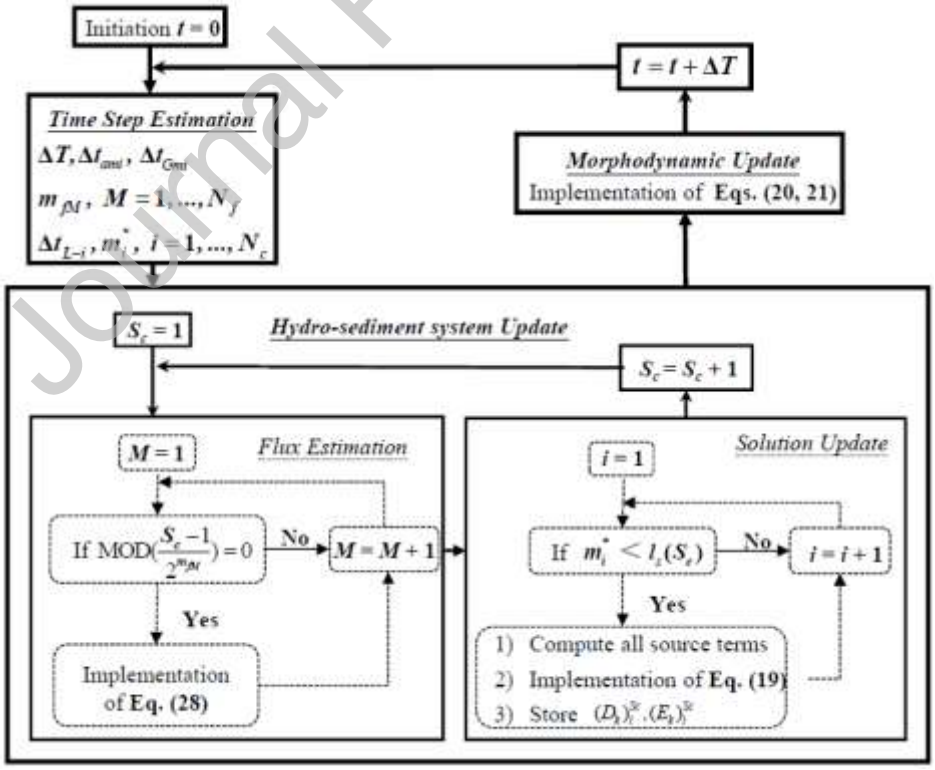

Figure 2. Numerical structure of for the new two-phase SHSM model

2.4 Estimation of numerical flux using the HLLC Riemann solver

Estimation of the inter-cell numerical fluxes (e.g., $\mathbf{E}_{nij}^{*}$ for the j-th face of the cell-i) is of high importance for high-resolution two-phase SHSM modeling. One aim of this paper is to apply the HLLC Riemann solver to estimate the numerical flux, which makes full use of the eigen-structures and thus is more accurate than the widely adopted centered schemes. To derive the eigenvalues, the governing equations are rewritten in the Jacobian matrix form as follows:

$$\frac{\partial \mathbf{U}}{\partial t}+\mathbf{J}(\mathbf{U})(\frac{\partial \mathbf{U}}{\partial x}+\frac{\partial \mathbf{U}}{\partial y})=\mathbf{S}_b+\mathbf{S}_\tau+\mathbf{S}_f+\mathbf{S}_s+\mathbf{S}_m \tag{24a}$$

with the Jacobian matrix reads:

$$\mathbf{J}(\mathbf{U})=\frac{\partial(\mathbf{F}n_x+\mathbf{G}n_y)}{\partial \mathbf{U}}=\begin{bmatrix}
0 & n_x & n_y & 0 & \cdots & 0 & 0 & \cdots & 0 & 0 & \cdots & 0 \\
a_{21} & a_{22} & a_{23} & 0 & \cdots & 0 & 0 & \cdots & 0 & 0 & \cdots & 0 \\
a_{31} & a_{32} & a_{33} & 0 & \cdots & 0 & 0 & \cdots & 0 & 0 & \cdots & 0 \\
0 & 0 & 0 & 0 & \cdots & 0 & n_x & \cdots & 0 & n_y & \cdots & 0 \\
\vdots & \vdots & \vdots & \vdots & & \vdots & 0 & n_x & \vdots & \vdots & n_y & \vdots \\
0 & 0 & 0 & 0 & \cdots & 0 & 0 & \cdots & n_x & 0 & \cdots & n_y \\
a_{51-1} & 0 & 0 & a_{54-1} & \cdots & 0 & a_{55-1} & \cdots & 0 & a_{56-1} & \cdots & 0 \\
a_{51-k} & \vdots & \vdots & \vdots & a_{54-k} & \vdots & \vdots & a_{55-k} & \vdots & \vdots & a_{56-k} & \vdots \\
a_{51-NSPS} & 0 & 0 & 0 & \cdots & a_{54-NSPS} & 0 & \cdots & a_{55-NSPS} & 0 & \cdots & a_{56-NSPS} \\
a_{61-1} & 0 & 0 & a_{64-1} & \cdots & 0 & a_{65-1} & \cdots & 0 & a_{66-1} & \cdots & 0 \\
a_{61-k} & \vdots & \vdots & \vdots & a_{64-k} & \vdots & \vdots & a_{65-k} & \vdots & \vdots & a_{66-k} & \vdots \\
a_{61-NSPS} & 0 & 0 & 0 & \cdots & a_{64-NSPS} & 0 & \cdots & a_{65-NSPS} & 0 & \cdots & a_{66-NSPS}
\end{bmatrix} \tag{24b}$$

where $a_{21}=ghn_x-uu_\perp$, $a_{22}=un_x+u_\perp$, $a_{23}=un_y$, $a_{31}=ghn_y-vu_\perp$, $a_{32}=vn_x$, $a_{33}=u_\perp+vn_y$, $a_{51-k}=\frac{\rho ghc_k n_x}{2\rho_s}$, $a_{61-k}=\frac{\rho ghc_k n_y}{2\rho_s}$, $a_{54-k}=\frac{\rho ghn_x}{2\rho_s}-u_{sk}u_{sk\perp}$, $a_{64-k}=\frac{\rho ghn_y}{2\rho_s}-v_{sk}u_{sk\perp}$, $a_{55-k}=u_{sk}n_x+u_{sk\perp}$, $a_{65-k}=\mathrm{v}_{sk}n_x$, $a_{56-k}=u_{sk}n_y$, $a_{66-k}=u_{sk\perp}+v_{sk}n_y$; and $u_{sk\perp}=u_{sk}n_x+v_{sk}n_y$, $u_\perp=un_x+vn_y$ are the velocities perpendicular to the cell face. The eigenvalues λ can be estimated from $|\mathbf{J}-\lambda\mathbf{I}|=0$ (where $\mathbf{I}$ is the unit matrix) and thus are the roots of the following characteristic polynomial:

$$(\lambda-u_{\perp})((\lambda-u_{\perp})^2-gh)\prod_{k=1}^{NSPS}\left[(\lambda-u_{sk\perp})((\lambda-u_{sk\perp})^2-\frac{\rho gh}{2\rho_s})\right]=0 \tag{25}$$

There are $3NSPS+3$ roots for Eq. (25), corresponding to the $3NSPS+3$ distinct eigenvalues. However, the HLLC Riemann solver was designed for 3-wave system. To overcome this challenge, these distinct eigenvalues are grouped into $NSPS+1$ parts: one part for the water-sediment mixture (Eq. 26), and NSPS part for the $NSPS$ sediment sizes (Eq. 27):

For the hydro-sediment mixture: $\lambda_1^{mixture}=u_{\perp}$, and

$$\lambda_{2,3}^{mixture}=u_{\perp}\pm\sqrt{gh} \tag{26}$$

For the k-th sediment phase: $\lambda_1^{Sed-k}=u_{sk\perp}$, and

$$\lambda_{2,3}^{Sed-k}=u_{sk\perp}\pm\sqrt{\frac{\rho gh}{2\rho_s}} \tag{27}$$

where $\lambda_{1,2,3}^{mixture}$ are eigenvalues related to the motion of the hydro-sediment mixture and $\lambda_{1,2,3}^{Sed-k}$ for the k-th sediment size, respectively. It is obvious from Eqs. (26, 27) that each part consists of three eigenvalues, which can be used to construct an independent 3-wave system and thus facilitates the implementation of the HLLC Riemann solver. Take the estimation of the numerical flux $\mathbf{E}_{nM}$ at the face-M as an example, the numerical flux should be also split into $NSPS+1$ parts (Eq. 28): one part for the hydro-sediment mixture ($\mathbf{F}_{HLLC}^{mixture}(\mathbf{W}_L,\mathbf{W}_R)$), and $NSPS$ part for the $NSPS$ sediment sizes ($\mathbf{F}_{HLLC}^{sed-k}(\mathbf{W}_L,\mathbf{W}_R)$, $k=1,\ NSPS$):

$$\mathbf{E}_{nM}=\begin{bmatrix}\mathbf{E}_{nM}^{\text{mixture}}\\ \mathbf{E}_{nM}^{sed-1}\\ \mathbf{E}_{nM}^{sed-k}\\ \mathbf{E}_{nM}^{sed-NSPS}\end{bmatrix}=\begin{bmatrix}\mathbf{F}_{HLLC}^{mixture}(\mathbf{W}_L,\mathbf{W}_R)\\ \mathbf{F}_{HLLC}^{sed-k}(\mathbf{W}_L,\mathbf{W}_R)\\ \mathbf{F}_{HLLC}^{sed-k}(\mathbf{W}_L,\mathbf{W}_R)\\ \mathbf{F}_{HLLC}^{sed-k}(\mathbf{W}_L,\mathbf{W}_R)\end{bmatrix} \tag{28}$$

where $\mathbf{W}_L,\mathbf{W}_R$ are the two conservative variable vectors at the left and right side of the face-M, which are used by the HLLC-type Riemann solver (see the Appendix); the subscripts

" L, R " indicates the left and right sides, respectively. For convenience in description, the three elements of the vector $\mathbf{W}$ are represented by w_1, $w_1 w_2$, and $w_1 w_3$:

For the mixture part:

$$w_1 \equiv h,\ w_2 \equiv u,\ w_3 \equiv v \tag{29}$$

For the k-th sediment size part:

$$w_1 \equiv hc_k,\ w_2 \equiv u_{sk},\ w_3 \equiv v_{sk} \tag{30}$$

In the present model, the first-order method is used by setting the Riemann states $\mathbf{W}_L, \mathbf{W}_R$ directly equal to the values of the conserved variables at the neighboring cell center. To ensure non-negative water depth reconstruction, the following modifications on the left and right Riemann states must be implemented (Audusse et al. 2004). Firstly, the bed elevations at two sides are estimated as follows:

$$z_{bML} = \eta_{bML} - h_{ML}, z_{bMR} = \eta_{bMR} - h_{MR} \tag{31a}$$

Secondly, the water depth at two sides are modified as:

$$h_{ML} = \max(0, \eta_{bML} - z_{bM}), h_{MR} = \max(0, \eta_{bMR} - z_{bM}) \tag{32b}$$

where $z_{bM} = \max(z_{bML}, z_{bMR})$.

The specific expressions for the classical HLLC-type Riemann solver can be found in the literature (Toro 2001, 2019) and in the Appendix. To demonstrate the advantages of the upwind HLLC solver for two-phase SHSM modeling, another two-phase SHSM model is also developed with the centered FORCE solver, for which no information of the eigenvalues and wave structures are needed. The details of the FORCE solver can also be found in the

Appendix.

3. Model Performance

To demonstrate the performance of the new two-phase SHSM model, convergence rate study is firstly conducted; afterwards, the new model is tested against a series of flow-sediment-bed evolutions due to (1) two refilling processes of dredged trenches (Van Rijn, 1986; Armanini and Di Silvio ,1988), (2) two instantaneous dam-break flooding flows (Spinewine and Zech, 2007; Soares-Frazão et al., 2012), and (3) one levee breaching process (Tingsanchali and Chinnarasri, 2001). It is appreciated that these flow scenarios have been intensively simulated by quasi-single phase SHSM models (Zhao et al. 2019; Juez et al. 2014; Meurice and Soares-Frazão 2020 and Hu et al. 2019) or two-phase SHSM models that are based on the centered schemes (Greco et al. 2012; Di Cristo et al. 2016). As compared to quasi-single phase SHSM models, the present new model can shed lights on the role of inter-phase interaction between water and sediment. For example, the velocity discrepancy between the sediment phase and the water phase can be resolved by the present two-phase SHSM model. However, such inter-phase interaction is ignored by the previous single-phase SHSM models. From a perspective of physics, this velocity lag may significantly alter bed topography evolution. Nevertheless, comparisons of numerical solutions between the quasi-single phase model and the two-phase model are not shown in this paper because the focus of this paper is to advance existing two-phase SHSM modeling capabilities. As compared to previous two-phase SHSM models, the present model features improvements in both numerical accuracy and the ability to capture

key flow features, which will be demonstrated in the following.

3.1. Convergence rate study

An idealized dam-break flow over a frictionless dry bed is simulated on successively refined meshes (the averaged mesh sizes are 0.2 m, 0.1 m, 0.05 m and 0.025 m, respectively): a square domain of [20, 1] m^2 is considered: the bed is initially dry for $x>0$ m, and the initial water depth h_0 for $x\le 0$ m is set to 0.6 m. The analytical solution for the water depth is as follows

$$h(x,y,t)=\begin{cases} h_0 & x\le x_A(t) \\ \dfrac{4}{9g}\left(\sqrt{gh_0}-\dfrac{x-x_0}{2t}\right)^2 & x_A(t)\le x\le x_B(t) \\ 0 & x\ge x_B(t) \end{cases} \quad (33)$$

where $x_A(t)=-t\sqrt{gh_0}$ and $x_B(t)=2t\sqrt{gh_0}$. Fig. 3 presents comparisons between the exact solutions and the numerical solutions (water depth) on successive refined meshes by the two-phase SHSM model using (a) the HLLC solver and (b) the FORCE solver. From Fig. 3, the computed water depth by both solvers agree with the analytical solutions quite well, for which the discrepancy between the numerical and the analytical solutions decreases as the mesh size is refined. Standard norms (L_1 and L_∞) between the computed and analytical solutions of the water depth are computed, based on which the relative convergence rates are estimated. Table 1 shows the mesh statistics (cell number, averaged cell sizes), the standard norms L_1, L_∞ and the relative convergence rates at $t=0.5\ s$. From Table 1, the orders (0.68, 0.73, 0.75) of accuracy of the HLLC solver are consistently higher than those (0.58, 0.65, 0.73) of the FORCE solver. Moreover, the discrepancies between numerical solutions and analytical solutions (e.g., about 1.61E-2, 2.71E-2, 4.49E-2, 7.2E-2 for different meshes) for the HLLC solver are consistently smaller than those (e.g., about 2.98E-2, 4.93E-2, 7.74E-2, 1.16E-1 for different meshes) for the FORCE solver. The computed convergence rates for dam-break flow problems using the HLLC solver is consistent with previous evaluations

(Prebeg et al. 2018; Daude et al. 2014).

Afterwards, a pure scalar advection process in a horizontal square domain of [10000, 1000] m^2 (Petti and Bosa, 2007) is numerically simulated on successively refined meshes (the averaged mesh sizes are 200 m, 100 m, 50 m, 25 m and 12.5 m, respectively). The bed slopes are $S_{bx} = -0.001,\ S_{by} = 0$; and the bed Manning roughness $n = 0.025$. At the upstream boundary a steady flow rate $q = 0.1243\ \mathrm{m}^2/\mathrm{s}$ is imposed to obtain a uniform flow: $h = \left(qn / \sqrt{(-S_{bx})}\right)^{3/5}$ and $u = q/h$. An initially distribution of scalar concentration is imposed at the domain:

$$c_0(x, y, 0) = 10e^{-0.5(\frac{x-1400}{264})^2} + 6.5e^{-0.5(\frac{x-2400}{264})^2} \quad (34)$$

which is a linear superposition of two Gaussian distribution, the first centred at 1400 m with a peak value of 10 m and the second centred at 2400 m with a peak value of 6.5; both having a standard deviation of 264 m. The analytical solution of the scalar concentration is $c(x, y, t) = c_0(x - ut, y, t)$. The simulation time is 9600 s. Fig. 4 illustrates comparisons between the analytical and numerical (at 9600 s) solutions of scalar concentration on successively refined meshes by the two-phase SHSM model using (a) the HLLC solver and (b) the FORCE solver. Table 2 summarizes the mesh statistics (cell number, averaged cell sizes), the standard norms L_1 and L_∞ , as well as the relative convergence rates. It is obvious from Fig. 4 and Table 2 that the HLLC solver is advantageous in simulating sediment advection process, as compared to the FORCE solver. Specifically, the order (about 0.32, 0.41, 0.58, 0.74; 0.24, 0.36, 0.53, 0.70) of the HLLC solver is higher than the order (about 0.32, 0.32, 0.31, 0.40; 0.17, 0.21, 0.25, 0.35) of the FORCE solver. The discrepancy (about 1.60E-01 for a mesh of 151040) between numerical solutions and analytical solutions for the HLLC solver is much smaller than that (about 4.04E-01 for a mesh of 151040) for the FORCE solver. This confirms previous understanding that a centred solver may spread solution when scalar transport is concerned (Canestrelli and Toro, 2012).

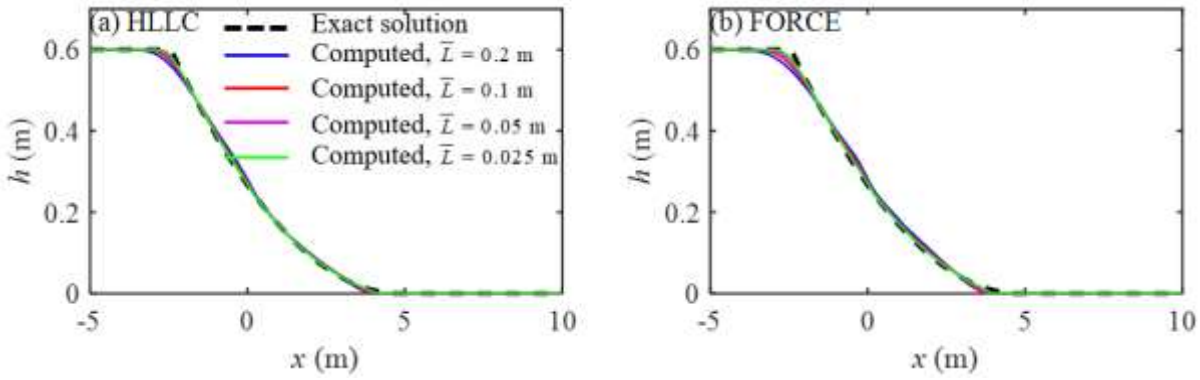

Figure 3. Comparisons between the analytical and numerical (at 0.5 s) solutions of water depth on successive refined meshes by the two-phase SHSM model using (a) the HLLC solver and (b) the FORCE solver

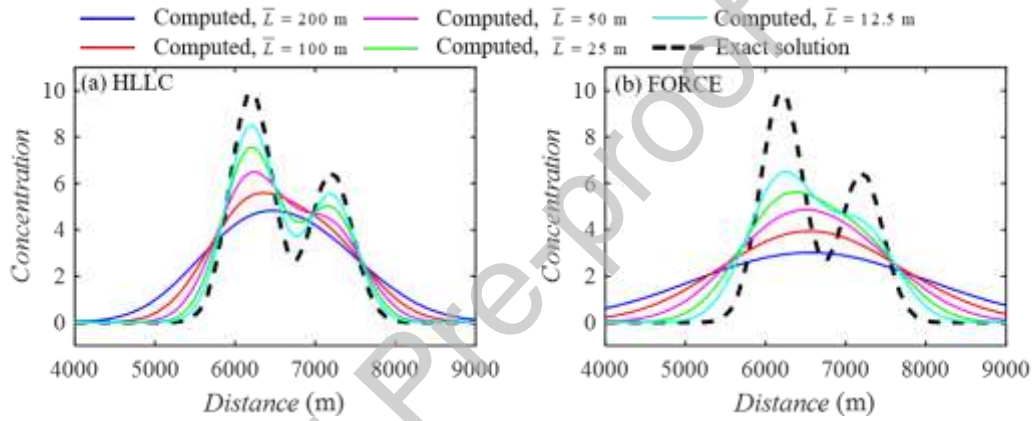

Figure 4. Comparisons between the analytical and numerical (at 9600 s) solutions of sediment concentration on successive refined meshes by the two-phase SHSM model using (a) the HLLC solver and (b) the FORCE solver

Table 1. Convergence rate study: error norms and experimental convergence rates.

Solver	N_c	$\overline{L}$ (m)	L_1	$O(L_1)$	L_∞	$O(L_\infty)$
HLLC	1010	0.2	7.20E-02		4.08E-02	
	4040	0.1	4.49E-02	0.68	3.06E-02	0.41
	16160	0.05	2.71E-02	0.73	2.34E-02	0.39
	64640	0.025	1.61E-02	0.75	1.67E-02	0.49
FORCE	1010	0.2	1.16E-01		5.23E-02	
	4040	0.1	7.74E-02	0.58	4.05E-02	0.37
	16160	0.05	4.93E-02	0.65	3.18E-02	0.35
	64640	0.025	2.98E-02	0.73	2.37E-02	0.42

Table 2. Convergence rate study: error norms and experimental convergence rates.

Solver	N_c	$\overline{L}$ (m)	L_1	$O(L_1)$	L_∞	$O(L_\infty)$
HLLC	590	200	6.61E-01		5.39E+00	
	2360	100	5.30E-01	0.32	4.56E+00	0.24
	9440	50	4.00E-01	0.41	3.55E+00	0.36
	37760	25	2.68E-01	0.58	2.46E+00	0.53

	151040	12.5	1.60E-01	0.74	1.52E+00	0.70
FORCE	590	200	1.03E+00		7.08E+00	
	2360	100	8.23E-01	0.32	6.30E+00	0.17
	9440	50	6.61E-01	0.32	5.45E+00	0.21
	37760	25	5.33E-01	0.31	4.59E+00	0.25
	151040	12.5	4.04E-01	0.40	3.60E+00	0.35

3.2. Refilling of dredged trench

Two scenarios about refilling of dredged trench are numerically simulated. The first scenario concerns the laboratory experiment carried out at a flume of dimensions 30 m length × 0.5 m width × 0.7 m height by van Rijn (1986) at Delft Hydraulics Laboratory (case 3.2.1). The geometry of the trench was 0.15 m depth with a slope gradient of 1:10. During the experiment, a constant unit inflow discharge of 0.2 m^2/s was specified at the inlet, with the mean flow depth and velocity stabilizing at 0.39 m and 0.51 m/s respectively. The bed was composed of fine sand (0.16 mm, 2650 kg/m^3) with a setting velocity of 0.013 m/s, a porosity of 0.4. The bed roughness is set to 0.011. During the experiment, equilibrium sediment transport was maintained at the inlet boundary, thus the corresponding equilibrium rate was 0.03 kg/m/s and the sediment concentration by weight at the cross section was 0.1508 kg/m^3. The sediment transport capacity is estimated by the Wu et al. (2000)'s formula with the threshold Shields parameter equal to 0.03, which is calibrated using the inlet sediment transport rate. The empirical parameter α is calibrated as 18. The computational domain covers the entire flume channel. Based on a sensitivity study on the mesh sizes, a total of 3084 triangular cells are used with an averaged cell size of 0.1 m.

Fig. 5 shows the bed elevation profiles computed by the models based on HLLC and FORCE solvers along with the measurements at $t =$ 7.5 h and 15 h. Despite the observed slight discrepancy between model predictions and measured data, the process of refilling of a dredged trench is well reproduced by the two models with bed aggradation due to sediment input occurring in the front end of the trench and bed degradation due to erosion appearing

around the tip of the rear edge of the trench. As time go on, a small amount of the sediment are gradually deposited at the bottom of the trailing edge, causing the slope gradient to gradually decrease. The relative discrepancy between model prediction and the measured data is quantified by $\sum_{i=1}^{N_{Mea}} \left|(\Delta z_{bi} - \Delta z_{bmi})\right| / \sum_{i=1}^{N_{Mea}} \Delta z_{bmi}$: the relative discrepancy is reduced from 9.56% for the FORCE solver to 6.36% for the HLLC solver. Note that this relation of relative discrepancy is used also in the following sections.

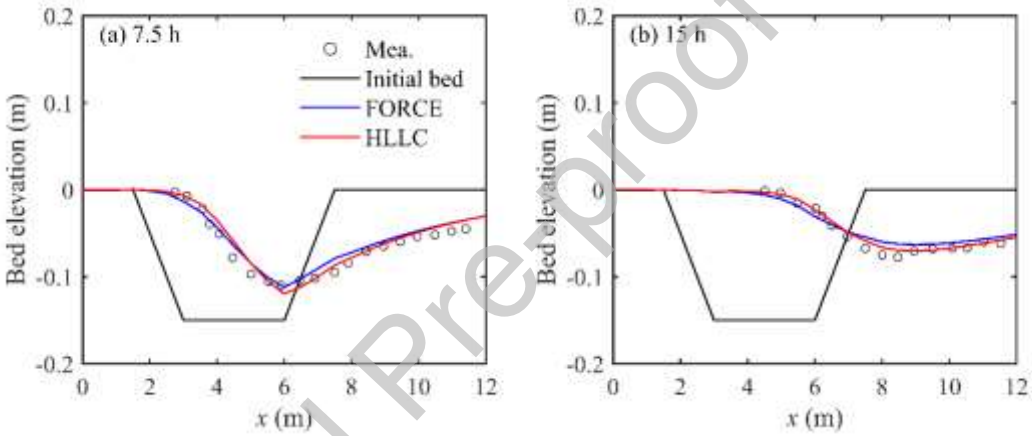

Figure 5. Refilling of a dredged trench: bed elevation profiles at (a) t= 7.5 h and (b) t= 15 h: model predictions by the HLLC solver (red lines) and the FORCE solver, as well as the superimposed measured data (open circles).

To further evaluate the capability of the two-phase model in modelling non-uniform sediment transport and morphological evolution, an extended case of trench refilling designed by Armanini and Di Silvio (1988) is revisited (case 3.2.2). In this case, a trench of the rather steep side slope (1:3) was set up and the sediment mixture consisted of two fractions: d_1 = 0.075 mm (50%) and d_2 = 0.3 mm (50%). The sediment density is 2650 kg/m^3. The unit inflow discharge was kept constant as 0.2 m^2/s. The computational domain covers the entire flume channel, therefore generating a total of 3084 triangular cells and 1853 nodes. The

following parameters are used (Li et al. 2019): $p_0 = 0.4$, $n = 0.011$, $a = 25$ and $\theta_c = 0.03$; the sediment transport capacity is estimated by the Wu et al. (2000)'s formula. Fig. 6 shows the bed elevation profiles computed by the models based on HLLC and FORCE solver along with the Armanini solution at $t =$ 7.5 h and 15 h. The process of refilling of a dredged trench can be also well reproduced by the two models which can demonstrate the two-phase models' ability to evaluate the non-uniform sediment transport. Rather limited differences in the bed profiles are observed for this case, featuring similar performances of the HLLC solver, FORCE solver and Armanini and Di Silvio (1988).

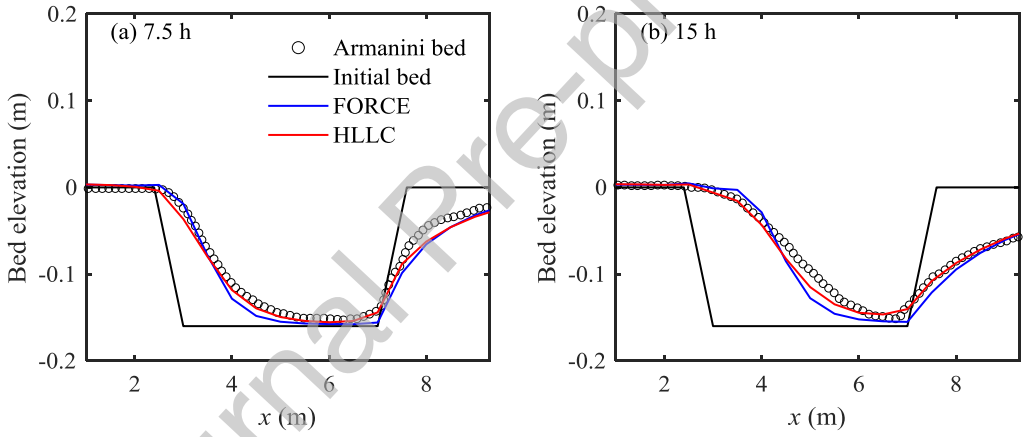

Figure 6. Refilling of a dredged trench for non-uniform sediment transport: bed elevation profiles at (a) t= 7.5 h and (b) t= 15 h: model predictions by HLLC solver (red lines) and FORCE solver (blue lines) and simulated data by Armanini and Di Silvio (1988) (open circles).

3.3. Instantaneous dam-break flooding flows and sediment transport

In this section, two scenarios about instantaneous dam-break flooding flows and sediment transport are numerically simulated. The first scenario (case 3.3.1) concerns full dam-break flows in an abruptly widening erodible channel, which was conducted at the Civil Engineering Laboratory of the Universite Catholique de Louvain (Spinewine and Zech,

2007): the 6 m-long flume has a sudden asymmetrical enlargement in the channel width from 0.25 m to 0.5 m at $x = 4$ m (Fig. 7). Dam break flows was created by the rapid removal of a thin gate, representing an idealized dam, which is located at the middle of the flume ($x = 3$ m). Initially, the bed was horizontal, composed of fully saturated non-cohesive sediments (diameter: 1.82 mm; density: 2680 kg/m^3; porosity: $p_0 = 0.47$) with a thickness of 0.1 m, and extended both sides of the gate. The initial water depth was 0.25 m upstream of the dam, and the bed was dry downstream of the dam. At the outlet of the flume, a weir was installed to control the downstream water level. Following previous calibration efforts (Hu et al. 2019), the MPM formula is used for the sediment transport capacity and the following parameters are used: bed roughness $n = 0.024$, $a = 10$ and $\theta_c = 0.047$. The computational domain covers the entire flume channel. Based on a sensitivity study on the mesh sizes, a total of 5182 triangular cells are used with an averaged cell size of 0.03 m. A free-slip, non-permeable condition was employed in the upstream boundary and side walls. It was observed during the course of the experiment that a hydraulic drop occurred downstream of the weir, so the outflow did not affect flow upstream of the weir. Hence, a transmissive condition was imposed at the downstream boundary. Measurements of stage time series and final bed topography were carried out at several gauges and cross sections. The measured data at three gauges, labelled P1, P2 and P3, and two cross sections, labelled CS1 and CS2 are selected to compare with the model predictions. The locations of P1, P2 and P3 as well as CS1 and CS2 were indicated in Fig. 7.

Fig. 8 shows water level time series computed from models using the HLLC and FORCE solvers as well as two-phase flow model of Greco et al. (2012), along with the measured data. In general, as the dam-break flow bore propagates downstream, water levels at gauges P1 and P3 undergoes a rapid initial rising followed by a gradual decrease. For the gauge P2 at the corner of the enlarged cross-section, water level experiences a relatively slow increase. As can be seen from Fig. 8, at gauge P1 which is immediately downstream of the dam, the water level time series predicted by the three model agree rather well with the observed data.

However, at P2 and P3 located in the abruptly widening area, the model using HLLC solver performs appreciably better than the other two models when compared to the measured data. This phenomenon demonstrates the superiority of HLLC solver in shock capturing.

Fig. 9 presents measured and computed bed level profiles from these aforementioned models. Although appreciable discrepancy can be identified, the model based on HLLC solver agrees well with the measured data as compared to the other models. This is further quantitatively confirmed by the relative discrepancy: the relative discrepancy by the HLLC solver (36.9% for CS1, 44.2% for CS2) is much smaller than those by the FORCE solver (64% for CS1, 60% for CS2) and those (45% for CS1, 65% for CS2) from Greco et al. 2012. Most notably, the discrepancy value of model based on HLLC solver is about 20% percent smaller than that of its counterpart using FORCE solver. Fig. 10 shows the contour plots of final bed deformation depth with flow velocity vectors for the water-sediment mixture and the sediment phase predicted by models based on HLLC solver and FORCE solver, respectively. Note that the velocity plots produced using the original triangular mesh look ugly. We have interpolated the velocity on structured meshes, based on which the velocity plots are produced. Both models have reproduced the phenomenon that intense bed erosion occurs downstream of the dam, and then the eroded sediments are deposited downstream of the right side of the enlarged cross-section and form a stripe of bed aggradation. Moreover, the depth-averaged velocity of the sediment phase is shown to be remarkably lower than that of the water-sediment mixture. According to the results by model using HLLC solver, a vortex is formed at the corner of the enlarged cross-section, whereas this behavior is not exhibited from the results due to model based on FORCE solver.

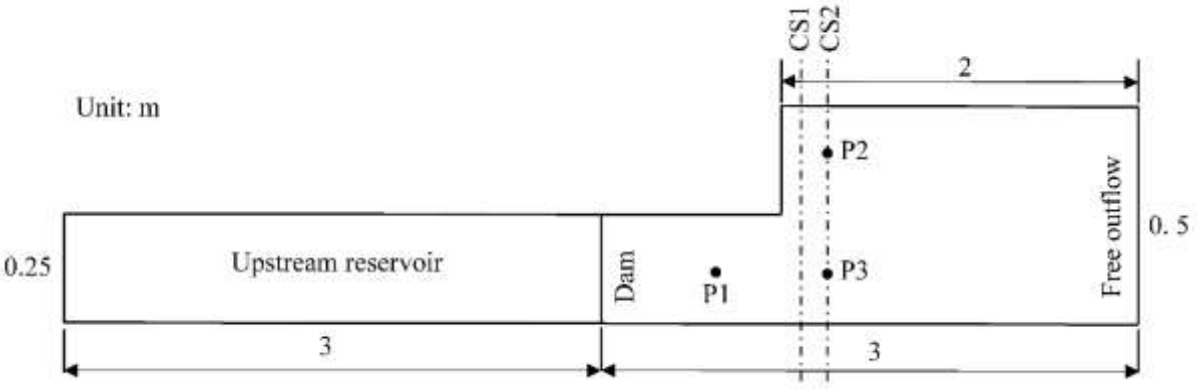

Figure 7. Sketch of the UCL dam-break experiment in a widening channel

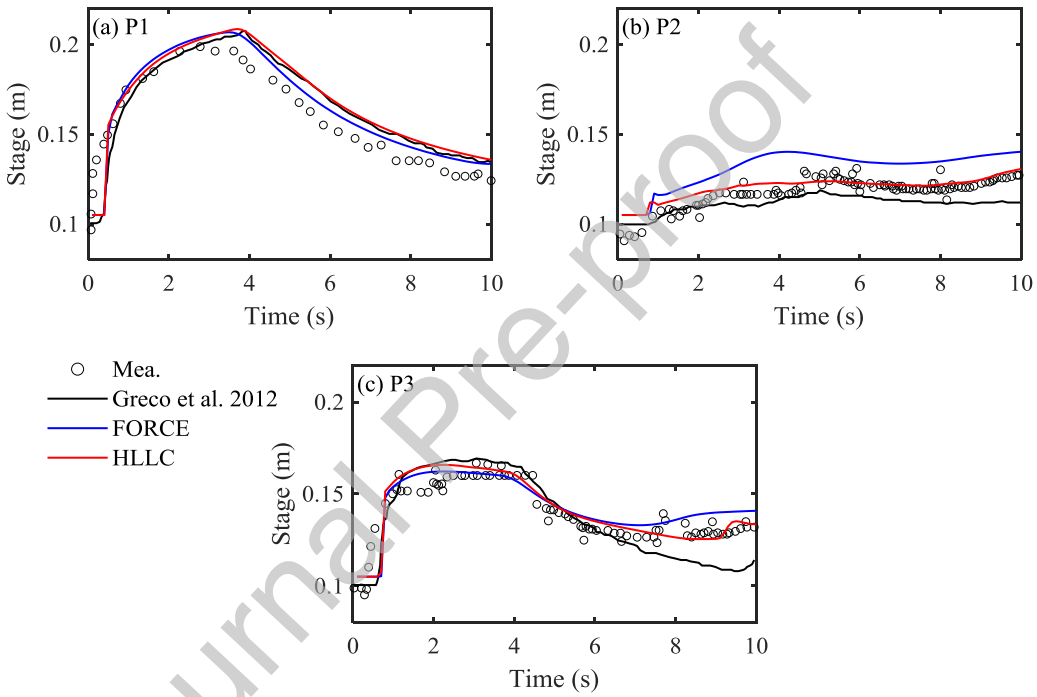

Figure 8. The full dam break scenario: computed and measured stage time series at three gauges: (a) P1, (b) P2 and (c) P3.

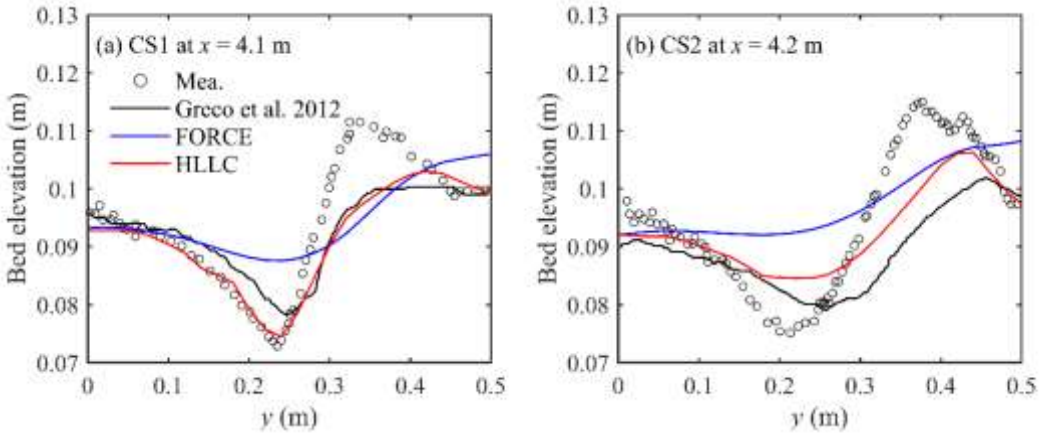

Figure 9. The full dam break scenario: computed and measured cross-sectional bed profiles

at (a) CS1 and (b) CS2.

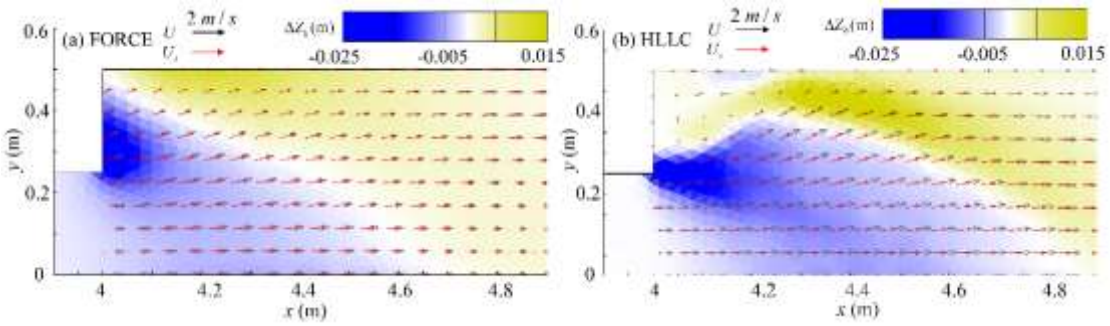

Figure 10. The full dam break scenario: model predictions of final bed deformation contours and flow velocity vectors for water-sediment mixture and sediment phase using (a) FORCE solver and (b) HLLC solver at t= 4 s.

The second scenario (case 3.3.2) concerns partial dam break flows in a straight erodible channel by Soares-Frazao et al. (2012). The flume is of 35 m length and 3.6 m width (Fig. 11). The partial dam break was created by rapid lifting the 1-m wide gate, which was originally located in the middle of the flume and between two imperious blocks. The rigid bed of the flume was covered by a 0.85 m-thick layer of fully saturated sands with median diameter 1.61 mm and density 2630 kg/m^3, which extended from 1 m upstream of the gate to 9 m downstream of the gate. The outlet of the flume consisted of a weir and sediment entrapment system. Initially, the water level inside the reservoir was 0.47 m and the downstream reach was dry. The experiment lasted for 20 s. Measurements of water levels and final bed elevations were conducted in two repeated experiment runs given the above experimental setup, labelled 'Mea. 1' and 'Mea. 2' respectively. Water level measurements were undertaken at eight gauges during the course of both experiment runs. Gauges 1-4 were located along x = 0.64 m, with y = -0.5, -0.165, 0.165 and 0.5 m, respectively. Gauges 5-8 were along x = 1.94 m , with y = -0.99, -0.33, 0.33 and 0.99 m. Bed elevation measurements were carried out at the end of the two experiments (i.e., t = 20 s), with data available for three longitudinal lines (y = 0.2, 0.7 and 1.45 m). Following calibrations by Hu et al. (2019): $p_0 = 0.47$, $n = 0.0165$ for the sand bed region and $n = 0.01$ for otherwise; and

parameter α is set equal to 5; the sediment transport capacity is estimated by the MPM relation with $\theta_c = 0.04$. The computational domain covers the entire flume channel with a total of 21440 triangular cells with the average cell size of 0.1 m.

Fig. 12 presents the computed water level time series at four gauges computed from the HLLC solver, the FORCE solver and Di Cristo et al. (2016), along with the measured data. In general, with the propagation of dam break flow toward to the outlet, water levels at all gauges undergo a rapid increase at the early stage and then decrease gradually. Fig. 13 shows the measured and predicted final bed elevation profiles along three longitudinal lines, i.e., (a) $y =$ 0.2 m, (b) $y =$ 0.7 m and (c) $y =$ 1.45 m from the aforementioned three models. In Fig. 13, considerable discrepancies between the two sets of measured bed elevation profiles are observed especially in the near downstream of the dam, although the two experiment runs are conducted under the same setup. It indicates the bed change near the dam region is very sensitive and uncertain even to trivial disturbances in doing the experiments. As can be seen from Figs. 12 and 13, less accurate results are observed in the near-downstream region of the dam. This is arguably because the flow region around the corners of the expansion are characterized by strong and complicated 3-D flow structure, which however cannot be well captured by the depth-averaged models. Moreover, as compared to the other models, numerical predictions of maximum values of bed scouring and deposited depth by HLLC model are closer to measured data. In the far downstream region where close agreement is observed between the two sets of measurement, the accuracy of the predicted bed level is much improved in all models. This is further quantitatively confirmed by the relative discrepancy: the relative discrepancy by the HLLC solver (about 62.5%) is much smaller than those by the FORCE solver (74.7%) and those (72.1%) from Di Cristo et al. (2016). Fig. 14 presents the flow velocity vectors for the water phase and the sediment phase at different time instants computed from HLLC sovler and FORCE sovler. In general, the water phase moves

faster than the sediment phase. At the early stage (i.e., $t = 2$ s), the velocity difference between the water and sediment phases is relatively small as the dam-break flow is energetic enough to carry the sediments at almost the same velocity. Later when the flow energy decreases (i.e., $t > 5$ s), such difference grows as the grains decelerate more rapidly and move slower as compared to the water phase. Comparatively, the HLLC model is able to capture the vortex when dam-break flow hits the sidewalls, echoing the findings from Di Cristo et al. 2016. However, the FORCE model fails to reproduce such behavior, possibly leading to the distortion of deposition and erosion.

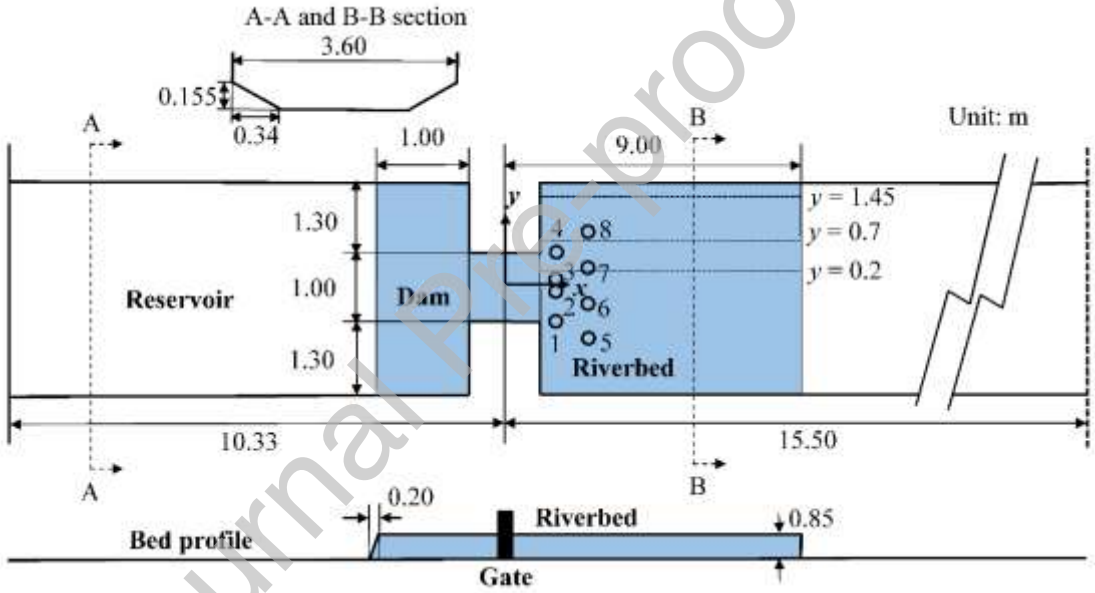

Figure 11. Sketch of the UCL partial dam-break experiment.

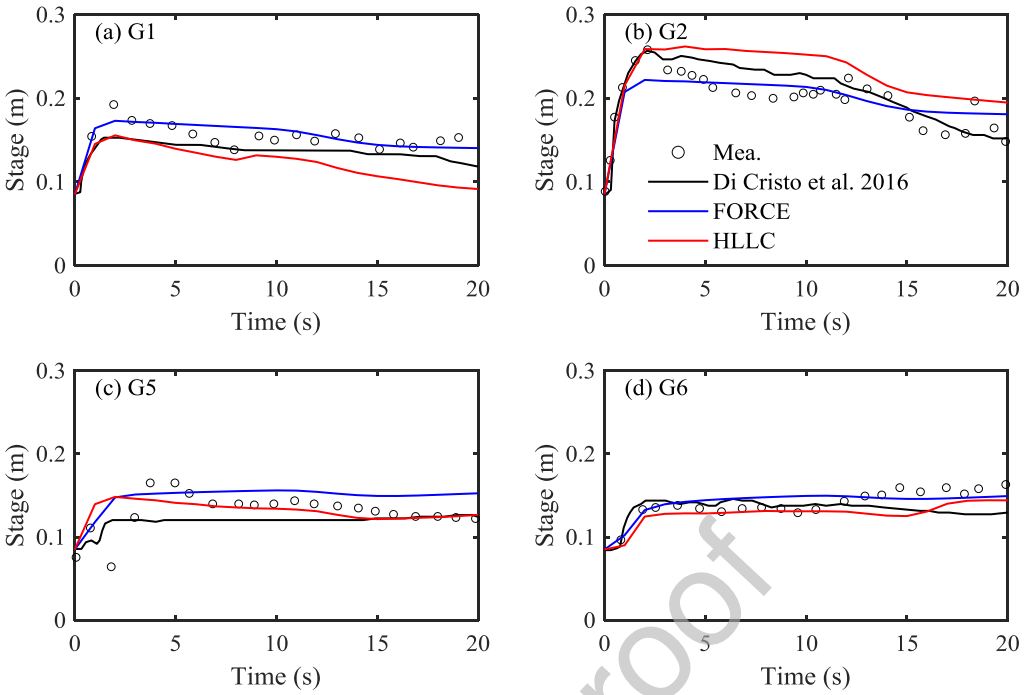

Figure 12. The partial dam break scenario: predicted (solid lines) and measured (open circles) water level time series at four gauges (a) G1, (b) G2, (c) G5 and (d) G6.

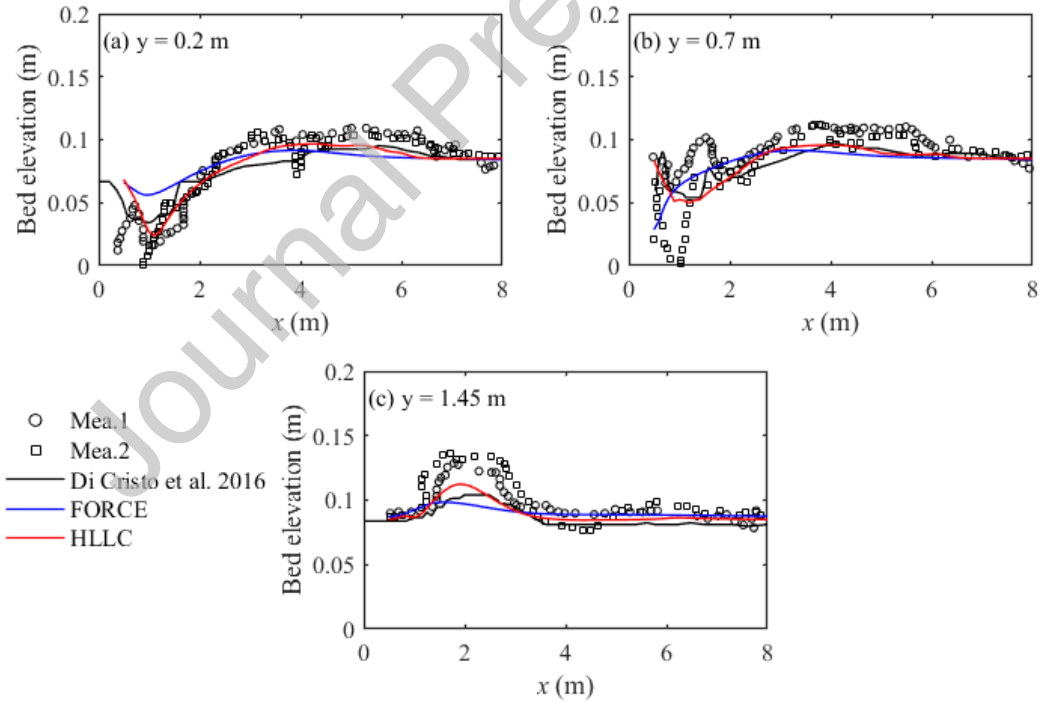

Figure 13. The partial dam break scenario: predicted (solid lines) and measured (open symbols) cross-sectional bed profiles at (a) y = 0.2 m; (b) at y = 0.7 m; (c) y = 1.45 m.

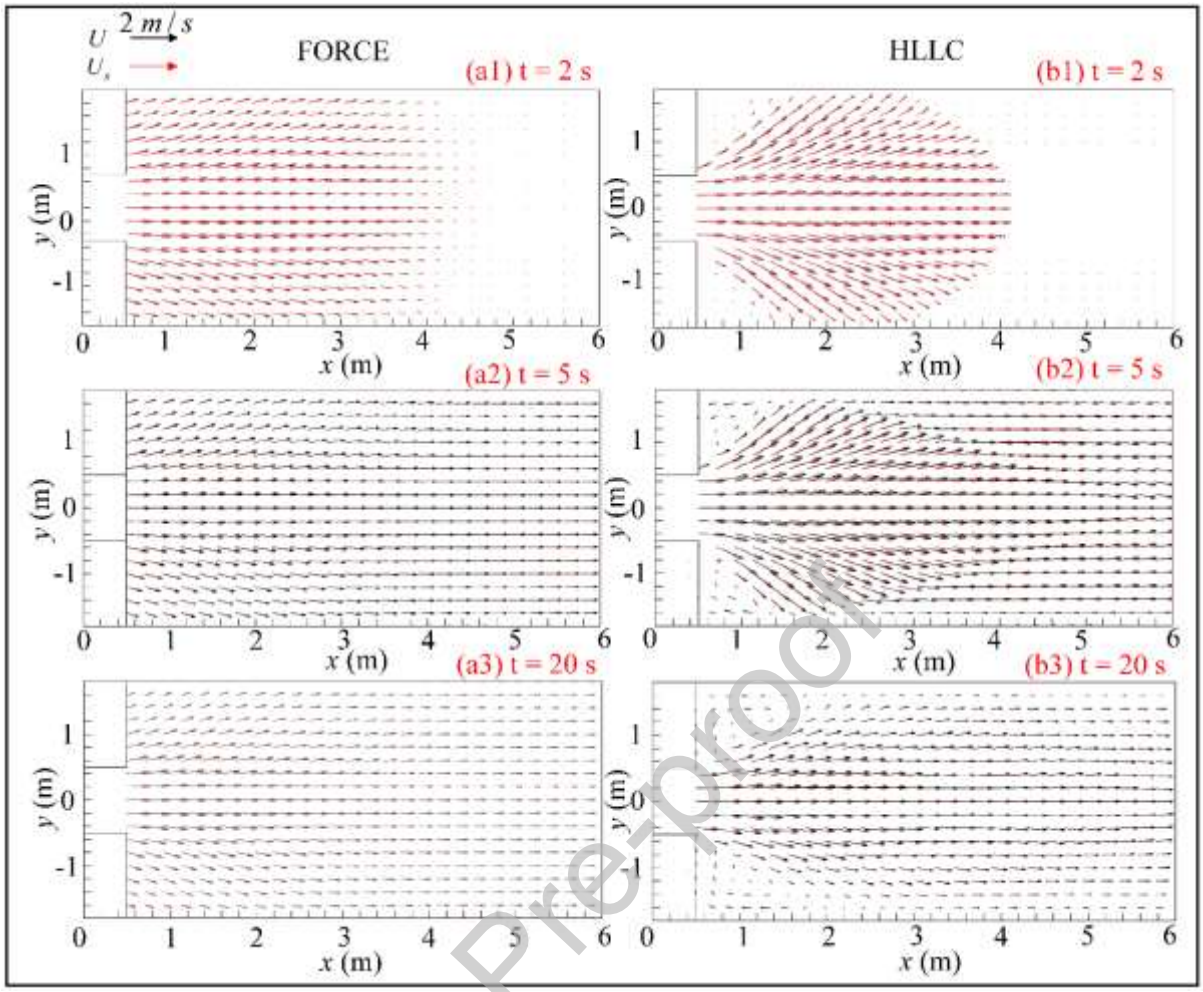

Figure 14. The partial dam-break scenario: model predictions of flow velocity vectors for water-sediment mixture and sediment phase by (a1-a3) the FORCE solver; and (b1-b3) the HLLC solver.

3.4. Levee breaching by overtopping flows

Here, the experimental levee breaching process by overtopping flows, which was reported by Tingsanchali and Chinnarasri (2001), is numerically simulated (case 3.4). This experiment has been widely applied to verify the performance of the hydro-sediment model (Wu and Wang, 2008, Zhao et al. 2019, Martínez-Aranda et al. 2019, Mahdizadeh and Sharifi, 2021). The flume is 35 m long and 1 m wide, a dyke of 0.8 m high and 1 m wide is placed at the middle of the flume with a crest width of 0.3 m. The upstream and downstream slopes of the dyke are 1:3 and 1:2.5 (See Fig. 15). The bottom of upstream and downstream of the dyke is fixed and unmovable, and the dyke is made of medium sand with a diameter of $d = 1.13\ mm$ and $\rho_s = 2650\ kg/m^3$. The sediment transport capacity is estimated by MPM formulation;

$p_0 = 0.47$, $n = 0.024$, $\alpha = h/\omega\Delta t$ and $\theta_c = 0.047$. Based on a sensitivity study on mesh sizes, a total of 5182 triangular cells and 2802 nodes is generated with an averaged size of 0.01 m. Fig. 16 presents the measured and computed (at 30 s and at 60 s) bed level profiles from these aforementioned quasi-single phase models and the present two-phase models. From Fig. 16, model predictions by the two-phase model with HLLC solver appears to agree better with the measured data as compared to the two-phase model with FORCE solver and other quasi-single-phase models. The averaged relative discrepancy is 19.06% for the two-phase model with the HLLC solver, whereas it is 35.27% for the two-phase model with the FORCE solver. As compared to these previous quasi-single phase models, the quantitative accuracy of the present two-phase model is not only satisfactory, but also can resolve the complex interactions between the water phase and the sediment phase.

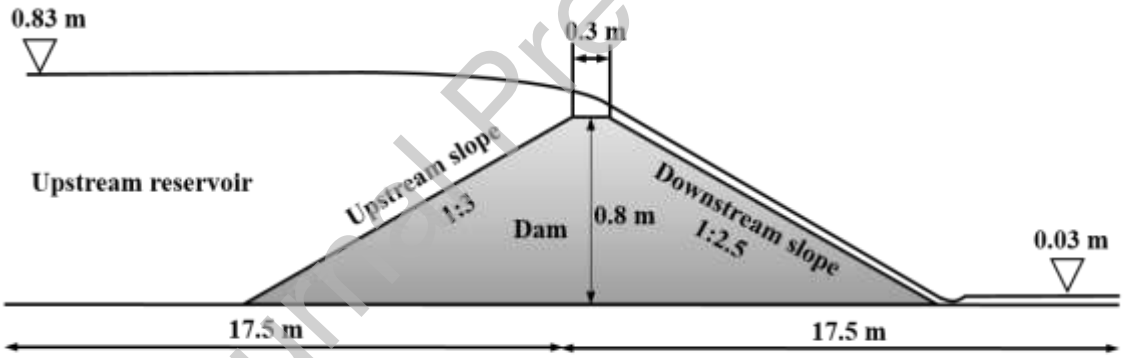

Figure 15. Sketch of the Levee breaching by overtopping flows.

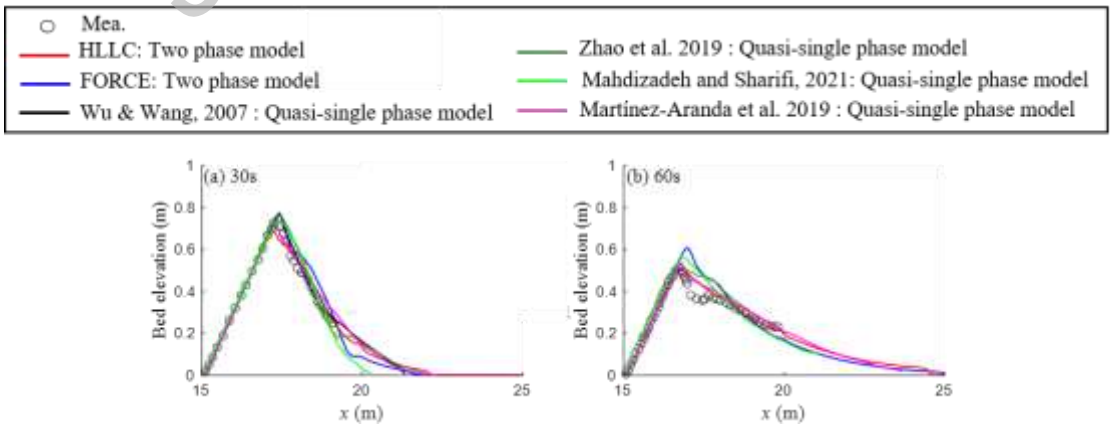

Figure 16. The levee breaching scenario: computed with HLLC, FORCE, Wu and Wang, (2008), Zhao et al. (2019), Martínez-Aranda et al. (2019), Mahdizadeh and Sharifi, (2021)

and measured bed profiles at (a) t = 30 s and (b) t = 60 s.

3.5. Evaluation of the computational efficiency

While the HLLC solver is more accurate than the FORCE solver, the former is more complex than the later (see the Appendix). Inevitably, this will induce some extra computational cost. Nevertheless, it is expected that the implementation of the hybrid LTS/GMaTS can overcome this extra computational cost. In this regard, computational cost of three versions of two-phase SHSM models are compared: the traditional version using the FORCE solver and the GMiTS, the present improved version using the HLLC solver and the hybrid approach, and an intermediate version using the HLLC solver and the GMiTS. Obviously, the intermediate version should be computationally most demanding. Therefore, computational costs of the other two versions is regularized against the intermediate version. The resultant statistics of the relative computational cost and the speed-ups of the other two versions are presented in Table 3. From Table 3, the following is observed. First, in terms of the computational efficiency, using the simple FORCE solver can only bring very negligible advantage over the complex HLLC solver: the speed-ups of the FORCE are about 1.07-1.1, which is negligible. Second, implementation of the hybrid LTS/GMaTS brings significant improvement in the computational efficiency: the corresponding speed-ups can be as high as 1.88 for the steady flow scenario (refilling of dredged channels) and 3.0-3.2 for unsteady flow scenarios (full and partial dam breaks, levee breaching). For simulations in Section 3.2-3.4, relatively uniform meshes are adopted. If the mesh is locally further refined, which is common for natural-scale simulations, more speed-ups can be expected.

Table 3. Summaries of the efficiency performances.

Test	Features of the model	Relative computational cost	Speed-ups
Case 3.2.1: Refilling dredged trench	GMiTS+HLLC	1.000	1.000
	GMiTS+FORCE	0.933	1.072
	Hybrid LTS/GMaTS+HLLC	0.532	1.880

Case 3.3.1: Full dam break	GMiTS+HLLC	1.000	1.000
	GMiTS+FORCE	0.910	1.099
	Hybrid LTS/GMaTS+HLLC	0.307	3.258
Case 3.3.2: Partial dam break	GMiTS+HLLC	1.000	1.000
	GMiTS+FORCE	0.920	1.083
	Hybrid LTS/GMaTS+HLLC	0.332	3.008
Case 3.4: Levee breaching	GMiTS+HLLC	1.000	1.000
	GMiTS+FORCE	0.918	1.090
	Hybrid LTS/GMaTS+HLLC	0.307	3.261

4. Conclusions

This paper presents a new depth-averaged two-phase flow model for hydro-sediment-morphodynamic processes, which is computationally-efficient and high-resolution based on the HLLC Riemann solver, a hybrid LTS/GMaTS approach. The two-phase SHSM models exhibits excellent potential for direct analysis of velocity lag between water and sediment phases and can exhibit encouraging performance as compared to the counterpart using centered FORCE solver and GMiTS approach when tested against several typical cases concerning flow-sediment-bed evolution. The HLLC solver performs much better than FORCE solver, in that it not only better captures complex flow behaviors of the water and sediment phases, but also appreciably reduces the discrepancy between numerical solution and measured data. Moreover, the implementation of the hybrid LTS/GMaTS approach significantly reduces run time and improves computational efficiency. Further reduction in computational cost is expected when the hybrid approach is combined with parallel computing strategy such as multi-GPU and high-performance computing (HPC) clusters.

The present work facilitates a promising modelling framework to shallow water-sediment

flows. Applications of the present model to hydro-sediment-morphodynamic processes in typical waterways of the Yangtze River, China are ongoing. Inevitably, the proposed model bears uncertainties arising from closures for boundary resistance and sediment exchange with the bed; these still require systematic fundamental investigations into the associated mechanisms.

Declaration of interests

The authors declare that they have no known competing financial interests or personal relationships that could have appeared to influence the work reported in this paper.

Acknowledgements

This research is supported by the National Natural Science Foundation of China (No. 12172331), the Changjiang Waterway Institute of Planning and Design, the Zhejiang Natural Science Foundation (LR19E090002) and the HPC Center OF ZJU (ZHOUSHAN CAMPUS).

Appendix A. the HLLC solver and the FORCE solver

Here we presented the specific expressions of the HLLC solver and the FORCE solver.

The HLLC solver reads:

$$\mathbf{F}_{HLLC}(\mathbf{W}_L,\mathbf{W}_R)=\begin{cases}\mathbf{E}_L & S_L\geq 0\\ \mathbf{E}_{*L} & S_L<0\leq S_{Mid}\\ \mathbf{E}_{*R} & S_{Mid}<0\leq S_R\\ \mathbf{E}_R & S_R\geq 0\end{cases} \tag{A.1}$$

where S_L S_R and S_{Mid} are three wave speeds computed by Eq. (A.2); $\mathbf{E}_L$, $\mathbf{E}_{*L}$, $\mathbf{E}_{*R}$, and $\mathbf{E}_R$ are four Riemann numerical fluxes estimated by Eqs (A.5). For the hydro-sediment mixture, the wave speed S_L and S_R on the left and right sides are as follows:

$$S_L = \begin{cases} \min(w_{\perp L} - \sqrt{g_L w_{1L}},\ w_{\perp *} - \sqrt{g^* w_{1*}}) & \text{if } w_{1L} > 0 \\ w_{\perp R} - 2\sqrt{g_R w_{1R}} & \text{if } w_{1L} = 0 \end{cases} \tag{A.2a}$$

$$S_R = \begin{cases} \min(w_{\perp R} + \sqrt{g_R w_{1R}},\ w_{\perp *} + \sqrt{g^* w_{1*}}) & \text{if } w_{1R} > 0 \\ w_{\perp L} + 2\sqrt{g_L w_{1L}} & \text{if } w_{1R} = 0 \end{cases} \tag{A.2b}$$

The intermediate contact wave speed S_{Mid} is calculated as follows：

$$S_{Mid} = \frac{w_{1R} S_L (w_{\perp R} - S_R) - w_{1L} S_R (w_{\perp L} - S_L)}{w_{1R} (w_{\perp R} - S_R) - w_{1L} (w_{\perp L} - S_L)} \tag{A.2c}$$

where $w_{\perp L,R} = \left(w_2 n_x + w_3 n_y \right)_{L,R}$ are the normal velocities, $w_{\perp *}$, w_{1*} are the modified value on both sides of the flux with average methods, which can be calculated as follows

$$w_{\perp *} = \frac{\sqrt{w_{1L}} w_{\perp L} + \sqrt{w_{1R}} w_{\perp R}}{\sqrt{w_{1L}} + \sqrt{w_{1R}}},\ w_{1*} = \frac{w_{1L} + w_{1R}}{2} \tag{A.3a, b}$$

The parameters $g_{L,R}$ and g^* in Eq. (A2) should be treated differently for the mixture part and for the sediment part, which are as follows:

For the mixture part: $g_{L,R} = g$, and $g^* = g$ (A.4a, b)

For the k-th sediment part: $g_{L,R} = \frac{\rho_{ML,R}}{2\rho_s c_{kML,R}} g,\ g^* = (\frac{\rho_{ML}}{4\rho_s c_{kML}} + \frac{\rho_{MR}}{4\rho_s c_{kMR}}) g$ (A.4c, d)

Numerical flux vectors in the Eq. (A.1) can be estimated as follows

$$\mathbf{E}_{L,R} = \begin{bmatrix} w_1 w_\perp \\ w_1 w_2 w_\perp + 0.5 g' w_1^2 n_x \\ w_1 w_3 w_\perp + 0.5 g' w_1^2 n_y \end{bmatrix}_{L,R},\ \mathbf{E}_{*L,R} = \begin{bmatrix} \mathbf{E}_{HLL}(1) \\ \mathbf{E}_{HLL}(2) n_x - w_{//} \mathbf{E}_{HLL}(1) n_y \\ \mathbf{E}_{HLL}(2) n_y + w_{//} \mathbf{E}_{HLL}(1) n_x \end{bmatrix}_{L,R} \tag{A.5a, b}$$

where $w_{//L,R} = (-w_2 n_y + w_3 n_x)_{L,R}$ represent tangential velocity, and the parameter g' in Eq. (A5) should also be treated separately for the mixture part and for the sediment part

For the mixture part: $g' = g$

(A.6a)

For the k -th sediment part: $g' = (\frac{\rho_{ML}}{2\rho_s c_{kML}} + \frac{\rho_{MR}}{2\rho_s c_{kMR}})g$

(A.6b)

The flux $\mathbf{E}_{HLL}$ is calculated from the HLL formula:

$$\mathbf{E}_{HLL} = \frac{S_R \bar{\mathbf{E}}(\mathbf{W}_L) - S_L \bar{\mathbf{E}}(\mathbf{W}_R) + S_L S_R (\mathbf{W}_R - \mathbf{W}_L)}{S_R - S_L} \tag{A.7a}$$

$$\begin{bmatrix} 1 & 0 & 0 \\ 0 & n_x & -n_y \\ 0 & n_y & n_x \end{bmatrix} \bar{\mathbf{E}}(\mathbf{W}_{L,R}) = \mathbf{E}(\mathbf{W}_{L,R}) \tag{A.7b}$$

The FORCE solver reads:

$$\mathbf{E}_{nM} = \mathbf{F}_{FORCE}(\mathbf{U}_{ML}, \mathbf{U}_{MR}) = \frac{1}{2}(\mathbf{F}_{MLF} + \mathbf{F}_{MLW}) \ , \ M = 1, ..., N_f \tag{A.8}$$

where $\mathbf{U}_{ML}, \mathbf{U}_{MR}$ are two Riemann states immediately at the left and right side of the face as conserved variables; $\mathbf{F}_{MLF}$, $\mathbf{F}_{MLW}$ represent the Lax-Wendroff flux and the Lax-Friedrichs flux, which can be estimated as follows

$$\mathbf{F}_{MLF} = \frac{A_{ML}\mathbf{Y}(\mathbf{U}_{MR})\bullet\mathbf{n}_M + A_{MR}\mathbf{Y}(\mathbf{U}_{ML})\bullet\mathbf{n}_M}{A_{ML} + A_{MR}} + \frac{2A_{ML}A_{MR}}{\Delta t_{L-i}(A_{ML} + A_{MR})\Delta L_M}(\mathbf{U}_{ML} - \mathbf{U}_{MR}) \tag{A.9a}$$

$$\mathbf{F}_{MLW} = \mathbf{Y}(\mathbf{U}_{MLW})\bullet\mathbf{n}_M \tag{A.9b}$$

$$\mathbf{U}_{MLW} = \frac{\mathbf{U}_{MR}A_{MR} + \mathbf{U}_{ML}A_{ML}}{A_{MR} + A_{ML}} + \frac{\Delta t_{L-i}\Delta L_M}{2(A_{MR} + A_{ML})}(\mathbf{Y}(\mathbf{U}_{ML}) - \mathbf{Y}(\mathbf{U}_{MR}))\bullet\mathbf{n}_M \tag{A.9c}$$

where $\mathbf{n}_M = (n_{Mx}, n_{My})$ represents the normal outward direction of the M -th face and $\mathbf{Y}(\mathbf{U}_{ML,R,LW})\bullet\mathbf{n}_M = \mathbf{F}(\mathbf{U}_{ML,R,LW})n_{Mx} + \mathbf{G}(\mathbf{U}_{ML,R,LW})n_{My}$; ΔL_M is the length of the M -th face. A_{ML}, A_{MR} denote the area of the triangle formed by the face and the cell center.

References

Armanini, A., and Di Silvio, G. (1988). A one-dimensional model for the transport of a sediment mixture in non-equilibrium conditions. *Journal of Hydraulic Research*. *26*(3), 275– 292.

Audusse, E., Bouchut, F., Bristeau, M., Klein, R., and Perthame, B. (2004). A fast and stable well-balanced scheme with hydrostatic reconstruction for shallow water flows. *SIAM Journal on Scientific Computing, 25*(6), 2050–2065.

Bakhtyar, R., Yeganeh-Bakhtiary, A., Barry, D. A., and Ghaheri, A. (2009). Two-phase hydrodynamic and sediment transport modeling of wave-generated sheet flow. *Advances in Water Resources, 32*, 1267-1283.

Canestrelli, A., and Toro, E. F. (2012) Restoration of the contact surface in FORCE-type centred schemes I: Homogeneous two-dimensional shallow water equations. *Advances in Water Resources,47*:88-99.

Chen, X., Li, Y., Niu, X., Li, M., Chen, D., and Yu, X. (2011). A general two-phase turbulent flow model applied to the study of sediment transport in open channels. *International Journal of Multiphase Flow*, *37*, 1099-1108.

Cao, Z., Hu, P., and Pender, G. (2011). Multiple time scales of fluvial processes with bed load sediment and their implications for mathematical modelling. *Journal of Hydraulic Engineering, 137*(3), 267-276.

Cao, Z., Xia, C., Pender, G., and Liu, Q. (2017). Shallow water hydro-sediment-morphodynamic equations for fluvial processes. *Journal of Hydraulic Engineering, 143*(5), 02517001.

Conde, D. A. S., Canelas, R. B., & Ferreira, R. M. L. (2020). A unified object-oriented framework for CPU+GPU explicit hyperbolic solvers. *Advances in Engineering Sofware, 148*, 102802.

Di Cristo, C., Greco, M., Iervolino, M., Leopardi, A., and Vacca, A. (2016). Two-dimensional two-phase depth-integrated model for transients over mobile bed. *Journal of Hydraulic Engineering ASCE*, *142*(2), 04015043.

Daude, F., Galon, P., Gao, Z., and Blaud, E. (2014). Numerical experiments using a HLLC-type solver with ALE formulation for compressible two-phase flows five-equation models with phase transition. *Computers and Fluids, 94*, 112-138.

Furfaro, D., and Saurel, R. (2015). A simple HLLC-type Riemann solver for compressible non-equilibrium two-phase flows. *Computers and Fluids*, *111*, 159-178.

George, D. L., Iverson, R. M. (2014). A depth-averaged debris-flow model that includes the effects of evolving dilatancy. II. Numerical predictions and experimental tests. *Proceedings of the Royal Society A Mathematical Physical and Engineering Sciences,*

470(2170), 20130820.

Gidaspow, D. (1994). Multiphase flow and fluidization: continuum and kinetic theory description. *Journal of Non-Newtonian Fluid Mechanics*, *55*(2), 207-208.

Gray, J., and Chugunov, V. (2006). Particle-size segregation and diffusive remixing in shallow granular avalanches. *Journal of Fluid Mechanic*s, *569*, 365-398.

Greco, M., Iervolino, M., Leopardi, A., and Vacca, A. (2012). A two-phase model for fast geomorphic shallow flows. *International Journal of Sediment Research*. *27* (4), 409–425.

Greimann, B., Lai, Y., and Huang, J.C. (2008). Two-dimensional total sediment load model equations. *Journal of Hydraulic Engineering*, *134* (8), 1142–1146.

Guy S. and Castelltort, S. (2006). Coupled model of surface water flow, sediment transport and morphological evolution. *Computers andGeosciences, 32*(10), 1600-1614.

Hill K., and Tan D. (2014). Segregation in dense sheared flows: gravity, temperature gradients, and stress partitioning. *Journal of Fluid Mechanics*, *756*, 54-88.

Hoey T., and Ferguson R. (1994). Numerical simulation of downstream fining by selective transport in gravel bed rivers: Model development and illustration. *Water Resources Research*, *30*(7), 2251-2260.

Hou, J., Liang, Q., Simons, F., and Hinkelmann, R. (2013). A 2D well-balanced shallow flow model for unstructured cells with novel slope source term treatment. *Advances in Water Resources*, *52*(2), 107–131.

Hu, P, Cao, Z., Pender, G., and Tan, G. (2012). Numerical modelling of turbidity currents in Xiaolangdi Reservoir, Yellow River, China. *Journal of Hydrology, 464-465*, 41-53.

Hu, P., Cao, Z., Pender, G., and Liu, H. (2014). Numerical Modelling of riverbed grain size stratigraphic evolution. *International Journal of Sediment Research*, 29(3), 329-343.

Hu, P., Han, J., Li, W., Sun, Z., and He, Z. (2018). Numerical investigation of a sandbar formation and evolution in a tide-dominated estuary using a hydro-sediment-morphodynamic model. *Coastal Engineering Journal*, 60(4), 466-483.

Hu, P., Lei, Y., Han, J., Cao, Z., Liu, H., and He, Z. (2019). Computationally efficient modeling of hydro-sediment-morphodynamic processes using a hybrid local time step/global maximum time step. *Advances in Water Resources*, *127*(MAY), 26-38.

Hungr, O., and Mcdougall, S. (2009). Two numerical models for landslide dynamic analysis. *Computers and Geosciences, 35*(5), 978-992.

Ingelsten, S., Mark, A., Jareteg, K., Kádár, R., & Edelvik, F. (2020). Computationally efficient viscoelastic flow simulation using a Lagrangian-Eulerian method and GPU-acceleration. *Journal of Non-Newtonian Fluid Mechanics, 279,* 104264.

Iverson, R. M., Logan, M., Lahusen, R. G., and Berti, M. (2010). The perfect debris flow? Aggregated results from 28 large-scale experiments. *Journal of Geophysical Research*

Earth Surface, 115(F3).

Martínez-Aranda, S., Murillo, J., & García-Navarro, P. (2022). A GPU-accelerated Efficient Simulation Tool (EST) for 2D variable-density mud/debris flows over non-uniform erodible beds. *Engineering Geology, 296*, 106462.

Murillo, J., and García-Navarro, P. (2012). Augmented versions of the HLL and HLLC Riemann solvers including source terms in one and two dimensions for shallow flow applications. J*ournal of Computational Physics, 231*(20), 6861-6906.

Juez, C., Murillo, J., and García-Navarro, P. (2014). A 2D weakly-coupled and efficient numerical model for transient shallow flow and movable bed. *Advances in Water Resources, 71*, 93-109.

Kim, J., Ivanov, V., and Katopodes, N. (2013). Modeling erosion and sedimentation coupled with hydrological and overland flow processes at the watershed scale. *Water Resources Research*,*49*(9), 5134–5154.

van Rijn, L. C (1986). Mathematical modeling of suspended sediment in non-uniform flows. *Journal of Hydraulic Engineering, 112*(6), 433-455.

Li J., Cao Z., Hu K., Pender G., and Liu Q. (2018). A depth-averaged two-phase model for debris flows over fixed beds. *International Journal of Sediment Research*, *33*(04): 462-477.

Li, J., Cao, Z., Qian, H., Liu, Q., and Pender, G. (2019). A depth-averaged two-phase model for fluvial sediment-laden flows over erodible beds. *Advances in Water Resources*, *129*(JUL.), 338-353.

Li, J., Cao, Z., Cui, Y., and Borthwick, A. (2020). Barrier lake formation due to landslide impacting a river: a numerical study using a double layer-averaged two-phase flow model. *Applied Mathematical Modelling*, *80*, 574-601.

Martínez-Aranda, S., Murillo, J. and García-Navarro, P. (2019). A comparative analysis of capacity and non-capacity formulations for the simulation of unsteady flows over finite-depth erodible beds. *Advances in Water Resources*. *130*, 91-112.

Mcardell, B. W., Bartelt, P., and Kowalski, J. (2007). Field observations of basal forces and fluid pore pressure in a debris flow. *Geophysical Research Letters*, *34*(7), L07406.

Meurice, R., and Soares-Frazão, S. (2020). A 2D HLL-based weakly coupled model for transient flows on mobile beds. *Journal of Hydroinformatics, 22*(5), 1351-1369.

Muste, M., Yu, K., Fujita, I., and Ettema, R. (2005). Two-phase versus mixed-flow perspective on suspended sediment transport in turbulent channel flows. *Water Resource Research. 41*(10), W10402.

Petti, M., and Bosa, S. (2007). Accurate shock-capturing finite volume method for advection-dominated flow and pollutant transport. *Computers and Fluids*, 36, 455-466.

Pitman, E., and Le, L., (2005). A two-fluid model for avalanche and debris flows. *Philosophical transactions. Series A, Mathematical, physical, and engineering sciences*,

363(1832), 1573-1601.

Prebeg, M., Flatten, T., and Muller, B. (2018). Large time step HLL and HLLC solvers. *ESAIM: Mathematical Modelling and Numerical Analysis, 52*(4), 1239-1260.

Pudasaini, S. (2012). A general two-phase debris flow model. *Journal of Geophysical Research*, *117*, F03010.

Sanders, B. F. (2008). Integration of a shallow water model with a local time step. Journal of hydraulic research, 46(4), 466-475.

Savage S. and Hutter K., (1989). The motion of a finite mass of granular material down a rough incline. *Journal of Fluid Mechanics*, *199*(-1):177-215.

Shi, H., Yu, X., and Dalrymple, R. A. (2017). Development of a two-phase SPH model for sediment laden flows. *Computer Physics Communications, 221*, 259-272

Shi, H., Si, P., Dong, P., and Yu, X. (2019). A two-phase SPH model for massive sediment motion in free surface flows, *Advances in Water Resources*, *129*, 80-98.

Soares-Frazão, S., Canelas, R., Cao, Z., Cea, L., Chaudhry, H. M., Moran, A. D., et al. (2012). Dam-break flows over mobile beds: experiments and benchmark tests for numerical models. *Journal of Hydraulic Research, 50*(4), 364-375.

Spinewine, B., and Zech, Y., (2007). Small-scale laboratory dam-break waves on movable beds. *Journal of Hydraulic Research*, *45* (sup1), 73–86.

Sweet, J., Richter, D. H., & Thain, D. (2018). GPU acceleration of Eulerian–Lagrangian particle-laden turbulent flow simulations. *International Journal of Multiphase Flow, 99*, 437-445.

Tingsanchali, T., and Chinnarasri, C. (2001). Numerical modelling of dam failure due to flow overtopping. *International Association of Scientific Hydrology Bulletin, 46*(1), 113-130.

Toro, E. (2001). Shock-capturing Methods for Free-Surface Shallow Flows. John Wiley, New York.

Toro, E. (2019). The HLLC Riemann solver. *Shock Waves*, 29, 1065-1082.

Toro, E., Hidalgo, A., and Dumbser, M. (2009). FORCE solvers on unstructured meshes I: Conservative hyperbolic systems. *Journal of Computational Physics*, *228*(9), 3368-3389.

Wu, W., and Wang, S., (2008). One-dimensional explicit finite volume model for sediment transport, *Journal of Hydraulic Research*, *46*(1), 87-98.

Wu, W., Wang, S. S. Y., and Jia, Y. (2000). Nonuniform sediment transport in alluvial rivers. *Journal of Hydraulic Research, 38*(6), 427-434.

Zech, Y., Soares-Frazão, S., Spinewine, B., and Le Grelle, N. (2008). Dam-break induced sediment movement: Experimental approaches and numerical modelling. *Journal of Hydraulic Research, 46*(2), 176-190.

Zhang, R. (1961). River Dynamics. *Industry Press, Beijing, China* (in Chinese).

Zhao, J., Özgen-Xian, I., Liang, D., Wang, T., and Hinkelmann, R. (2019). A depth-averaged non-cohesive sediment transport model with improved discretization of flux and source terms. *Journal of Hydrology, 570*, 647-665.